LITHOS 514–515 (2025) 108188

Contents lists available at ScienceDirect

LITHOS

journal homepage: www.elsevier.com/locate/lithos

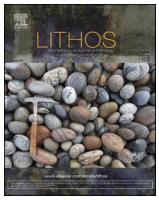

Age and geology of granitoids in northeast Palmer Land, Antarctic Peninsula

Ryan North [a,b,*], Lloyd T. White [a], Teal R. Riley [c], Dominique Tanner [a], Timothy T. Barrows [d]

[a] Environmental Futures Research Centre, School of Earth, Atmospheric and Life Sciences, University of Wollongong, Wollongong, NSW 2522, Australia
[b] Securing Antarctica's Environmental Future, University of Wollongong, Wollongong, NSW 2522, Australia
[c] British Antarctic Survey, High Cross, Madingley Road, Cambridge CB3 0ET, UK
[d] Chronos Radiocarbon Laboratory, Mark Wainwright Analytical Centre, University of New South Wales, Sydney 2052, Australia

ARTICLE INFO

Keywords:
West Antarctica
Gondwana
Zircon
Geochronology
Magmatism
Subcordilleran Plutonic Belt

ABSTRACT

The Antarctic Peninsula preserves a long history of Late Paleozoic and Mesozoic magmatism that reflects dynamic processes along the southwestern Gondwanan convergent margin. Granitoid magmatism is widespread across the Peninsula and records a complex history of subduction, massive silicic volcanism, and metamorphism. However, direct field observations are rare due to the inaccessibility of many remote outcrops, particularly in the central sector of the Antarctic Peninsula. Robust petrochronological data are even more scarce, limiting the ability to connect rock exposures across large ice-covered areas. Plutonic rocks across parts of the southern Antarctic Peninsula (northeast Palmer Land) lack detailed characterisation and geochronological constraints. Here, U—Pb isotopes and trace elements (e.g., Ti, P, Ce, Eu, and other REEs) are analysed in zircon ($n = 1148$) from archived samples from Mount Faith, Mount Sullivan, and Engel Peaks to calculate the timing and nature of magmatic and metamorphic events. These data are supplemented with in situ and whole-rock geochemistry. The resulting magmatic crystallisation ages are Early Jurassic (188–179 Ma) for calc-alkaline, peraluminous, weakly S-type granitoids at all three locations. This novel age constraint for the Mount Faith Granite: (1) indicates it is distinct from all three granitoid emplacement phases at Mount Charity immediately south, and (2) provides an upper age limit on cross-cutting tholeiitic mafic dykes. Deformation of the Mount Faith Granite could reflect either post-crystallisation strain or *syn*-emplacement strain that deformed granitoids of the Subcordilleran Plutonic Belt. Early Cretaceous (116–120 Ma) recrystallisation of Early Jurassic zircon provide evidence of the first phases of the Palmer Land Event on the central Peninsula. New data presented here provide a detailed geochronology of granitoids in northeast Palmer Land that can be used for Mesozoic tectonic reconstructions.

1. Introduction

The Antarctic Peninsula hosts diverse lithologies generated by its long-lived position in a complex tectonic setting along the former convergent margin of Gondwana (Jordan et al., 2020). The geology of northeast Palmer Land on the southern Antarctic Peninsula records several key igneous and deformation events that include Paleozoic-Triassic metamorphism, Mesozoic magmatism, Mesozoic-Cenozoic sedimentary units, and significant deformation and dyke emplacement during the Cretaceous related to large-scale tectonic adjustments (Burton-Johnson and Riley, 2015; Vaughan et al., 2012a, 2012b). This geological diversity is revealed only in relatively small, isolated outcrops which means it is difficult to generalise across large ice-covered regions. The remoteness of outcrops in northeast Palmer Land also mean that field-based geological observations are rare and thorough petrological and geochronological analyses are even rarer or non-existent for many parts of the Peninsula. However, archived geological samples at the British Antarctic Survey record over 60 years of geological activities across the Antarctic Peninsula and include material collected from areas that are difficult to access today as a result of retreating glaciers.

Petrological and geochemical analyses of rocks can provide insights into magmatic and tectonic histories. Whole-rock samples can be classified using in situ mineral relationships or bulk geochemical indices to reveal details about their geological history (e.g., Passchier and Trouw, 2005; Pearce et al., 1984). Zircon crystals, which can be extracted from crushed rock samples, record their timing of crystallisation and parent

* Corresponding author at: 1 Northfields Avenue, University of Wollongong, Wollongong, NSW 2522, Australia.
E-mail address: rnorth.academic@gmail.com (R. North).

https://doi.org/10.1016/j.lithos.2025.108188
Received 24 January 2025; Received in revised form 10 July 2025; Accepted 11 July 2025
Available online 16 July 2025

magma chemistry by absorbing different proportions of trace elements (e.g., U, Th, Ce, Eu, Ti, P, and other REEs) into their structure (Belousova et al., 2002; Belousova et al., 2006; Burnham and Berry, 2017; Loucks et al., 2020; Watson et al., 2006). Like detrital zircon is used to infer the age and properties of its original host rock (Belousova et al., 2002), so too can zircon from already-crushed rocks.

Hence, this study presents analyses of rock samples from Mount Faith, Mount Sullivan, and Engel Peaks in northeast Palmer Land to: (1) classify the local geology by providing new petrological descriptions and synthesising previous observations, and (2) precisely constrain the timing and nature of crystallisation of intrusive granitoids and metamorphic derivatives. Where whole-rock samples were available, optical and scanning electron microscopy were used to characterise their petrology in situ, and bulk rock compositional data were obtained using X-ray fluorescence spectroscopy. The primary mineralogy of samples was also identified using powder X-ray diffraction. Zircon was extracted to analyse U—Pb isotopes for radiometric dating and trace element concentrations for parent magma chemistry. Here, we present the first petrochronological characterisation of the Mount Faith Granite and improve the understanding of northern Palmer Land geology. The new data will aid sub-ice sheet correlations between isolated outcrops and provide robust constraints on the timing and location of subduction-related granitoid emplacement which are significant for tectonic reconstructions of the southwestern margin of Gondwana.

2. Geology of the Antarctic Peninsula

The Antarctic Peninsula evolved due to the convergence of paleo-Pacific oceanic (Phoenix) plate with the continental margin of Gondwana during the Phanerozoic (Jordan et al., 2014; Jordan et al., 2020; Riley et al., 2001; Riley et al., 2020; Riley et al., 2023). The complex magmatic, metamorphic, and accretionary history observed on the Antarctic Peninsula can be explained by subducting slab dynamics on a long-lived, para-autochthonous continental margin (Riley et al., 2023). Earlier interpretations describe the Peninsula as a composite of autochthonous and allochthonous terranes that merged during a major plate reorganisation during the Cretaceous (Vaughan et al., 2012a; Vaughan and Storey, 2000), but paleomagnetic data only supports a geological history where terranes developed in situ (Burton-Johnson and Riley, 2015; Gao et al., 2021).

Plutonic rocks comprise about half of the bedrock on the Peninsula and were emplaced during episodic peaks of magmatic activity mostly in the Permian, Jurassic and Cretaceous (Jordan et al., 2020; Leat et al., 1995; Riley et al., 2018; Riley et al., 2023). Arc magmatism in the Permian (280–250 Ma) was dominated by continental crust recycling, synchronous with widespread magmatism along the proto-pacific Gondwanan margin (Jordan et al., 2020). Four phases of magmatism occurred during the late-Triassic and Jurassic that emplaced granitoids on the Peninsula and Patagonia (V0: 223–200 Ma, V1: ~189–178 Ma, V2: ~173–160 Ma, and V3: 157–145 Ma; Bastias et al., 2021; Pankhurst et al., 2000). Several major tectonic events are coeval during the Early Jurassic (V1) peak of activity. Felsic volcanics were emplaced on the Peninsula and South America in the Chon Aike silicic large igneous province (LIP) which may be genetically related to processes that generated the coeval Karoo and Ferrar basaltic LIPs and led to the breakup of Gondwana (Bastias et al., 2021; Ivanov et al., 2017; Navarrete et al., 2024; Pankhurst et al., 1998; Pankhurst et al., 2000). Synchronous with magmatism of the Early Jurassic Chon Aike Province, 'normal' subduction-related granitoid magmatism has been identified along the Antarctic Peninsula (Riley et al., 2017) as a continuation of the Subcordilleran Plutonic Belt (Rapela et al., 2005).

Large volumes of plutonic rocks intruded the Peninsula and South America in magmatic 'flare-ups' during the Cretaceous (Bastias et al., 2022; Jordan et al., 2020; Leat et al., 1995; Paterson and Ducea, 2015; Riley et al., 2018), one of the most voluminous being the 130–102 Ma Lassiter Coast Intrusive Suite (LCIS) on the southern Peninsula (Riley et al., 2018). Initial emplacement of the LCIS correlates with the Palmer Land Event (116–103 Ma), a period of large-scale metamorphism and compressional deformation expressed as shearing, mylonitisation and brecciation of crystalline rocks in the Eastern Palmer Land Shear Zone ('EPLSZ'; Meneilly, 1988; Vaughan et al., 2002, 2012b). Calc-alkaline dyke swarms intrude basement rocks at ~100–97 Ma across Palmer Land and are related to the waning of the Palmer Land Event (Vaughan et al., 2012b). Arc-related magmatic and tectonic activity ceased by 20 Ma although subduction continues and rift-related magmatism on the northern Peninsula is ongoing (Jordan et al., 2020).

3. Local geology of Mount Faith, Mount Sullivan, and Engel Peaks

The Eternity Range in northern Palmer Land hosts the highest peaks on the Antarctic Peninsula in a ~ 45 km chain from north to south: Mount Faith (2838 m), Mount Hope (3248 m), and Mount Charity (2973 m). Limited bedrock is exposed above the ice sheet although long, narrow ridges radiate from the three main peaks. The peak of Mount Sullivan (2236 m) lies ~23 km east of the Mount Faith and itself a long (~13 km) series of arêtes and ridges oriented NE-SW. On the eastern coast of Palmer Land, three high-relief nunataks comprise Engel Peaks though samples are only available from 'South Engel Peak' (1398 m) here (Fig. 1).

The most up-to-date geological map ('GeoMAP') of Antarctica broadly captures the complex geology of Mount Faith, Mount Sullivan and Engel Peaks but compromises local detail for continent-scale coverage (Cox et al., 2023). More descriptive but scarce observations exist in unpublished BAS field reports (British Antarctic Survey, 1967, 1971a, 1971b, 1989, 2002) and in several publications (Davies, 1984; Meneilly, 1988; Scarrow et al., 1996; Vaughan et al., 2002; Vaughan et al., 2012b). However, the reported observations are not located precisely and geochronological constraints are sporadic. The known local geology from previous work is summarised below.

Unlike other peaks of the Eternity Range, there are only a few descriptions of Mount Faith. GeoMAP describes Mount Faith as a suite of felsic intrusive rocks of Early Jurassic to Early Cretaceous age, including varieties of granite, granophyre and quartz-feldspar porphyry (Cox et al., 2023). The bulk of exposed rock on all flanks of Mount Faith is described as a medium-grained, homogenous granitoid (British Antarctic Survey, 1967, 1971a, 1971b, 1989, 2002). Vertically dipping, 0.1–4 m wide mafic dykes commonly cross-cut the granitoid body. Other observations on Mount Faith flanks include rhyolites, pegmatites, aplite dykes, and meta-tuffs cross-cut and hornfelsed by granitic intrusions. Some of the granitoids also show evidence of deformation.

Specifically, the northeastern spur of Mount Faith where samples were selected for this study has been described as 'foliated granite' with large, pink euhedral orthoclase phenocrysts in a groundmass of anhedral plagioclase, quartz and mafic minerals (British Antarctic Survey, 1971b). Another description suggests a 'coarse grained, foliated hornblende granodiorite' (British Antarctic Survey, 2002). This granitoid has not been radiometrically dated but must be older than cross-cutting mafic dykes that are present here (and likely those that are found across eastern Palmer Land). Dykes were emplaced in two phases: (1) likely Late Triassic-Early Jurassic N-S striking tholeiitic dykes from shallow melting of fractionated sub-arc mantle subject to deformation, and (2) mid-Cretaceous *E*-W cross-cutting calc-alkaline dykes from deeper, more primitive mantle melting associated with Phase 2 of the Palmer Land Event (Vaughan et al., 2012a, 2012b). No published studies have characterised the Mount Faith Granite.

Mount Sullivan has received more attention due to its position within the EPLSZ (Fig. 1; Vaughan et al., 2002). Broadly, three major orogenies outcrop here: (1) Ordovician-Triassic crystalline metamorphic basement including quartzofeldspathic gneisses, garnetiferous restitic gneisses, and migmatites (British Antarctic Survey, 1971b; Burton-Johnson and Riley, 2015; Davies, 1984; Vaughan et al., 2002), (2) Early Jurassic

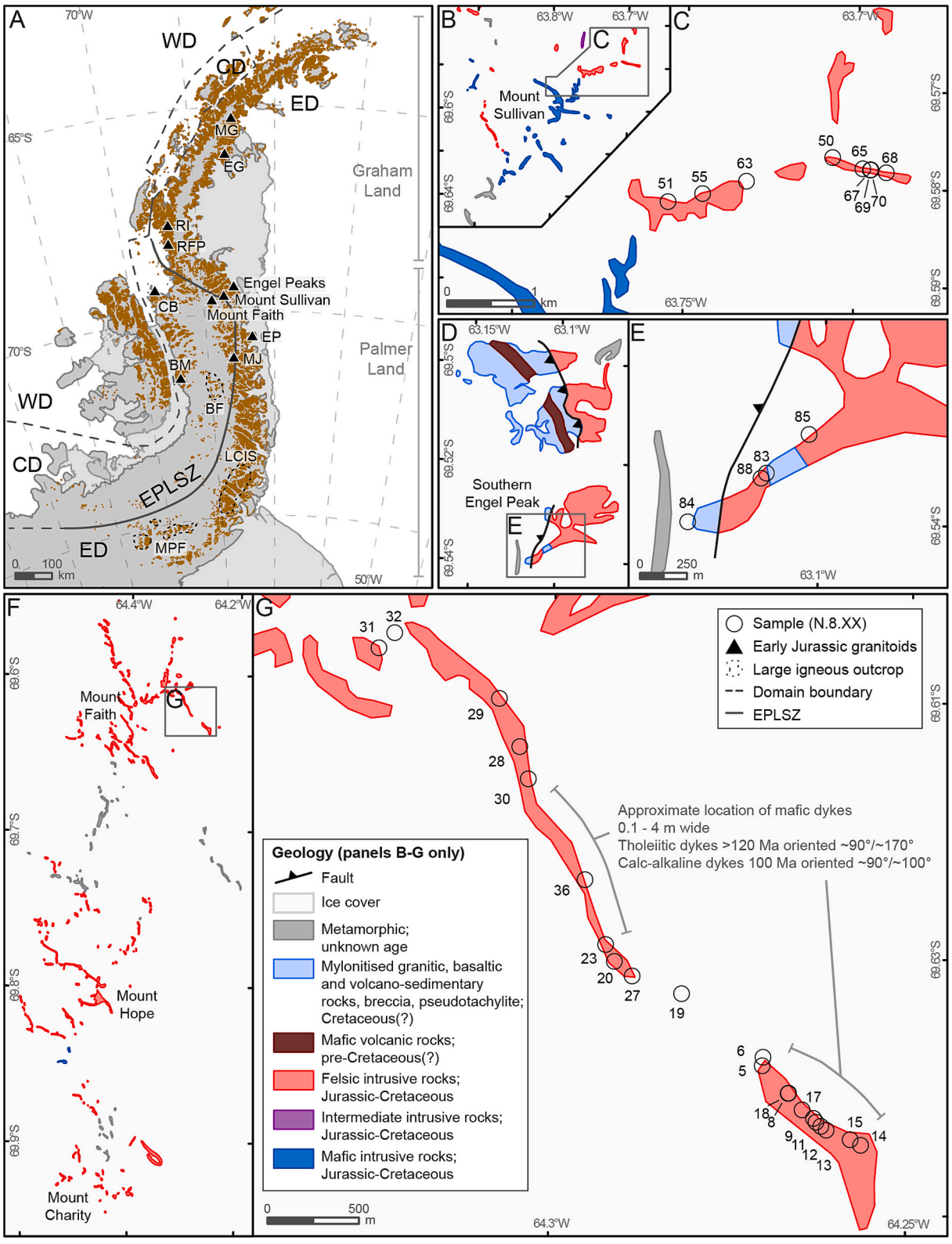

Fig. 1. (A) Rock exposure on the Antarctic Peninsula (Cox et al., 2023), study site locations, and other sites discussed in text: WD – Western Domain, CD – Central domain, ED – Eastern Domain, EPLSZ – Eastern Palmer Land Shear Zone, BF – Brennecke Formation, BM – Batterbee Mountains, CB – Cape Berteaux, EG – Eden Glacier, EP – Eielson Peninsula, LCIS – Lassiter Coast Intrusive Suite, MG – Mapple Glacier, MJ – Mount Jackson, MPF – Mount Poster Formation, RFP – Roman Four Promontory, RI – Reluctant Island. (B, C) Mount Sullivan simplified geology (Cox et al., 2023) and sample locations. (D, E) Engel Peaks simplified geology (Cox et al., 2023; Meneilly, 1988) and sample locations. (F, G) Eternity Range simplified geology (Cox et al., 2023) and sample locations. Mafic dyke information from (Vaughan et al., 2012b).

plutonic rocks that intruded through metamorphic basement including gabbros, porphyritic diorites, porphyritic granodiorites and granites, all of which are variably deformed and metamorphosed up to amphibolite facies (Davies, 1984; Pankhurst, 1983; Riley et al., 2017; Vaughan et al., 2002), and (3) mid-Cretaceous high-strain, high-temperature ductile shearing producing proto- to ultra-mylonites and pseudotachylites related to Phase 2 of the PLE (Vaughan et al., 2002; Vaughan et al., 2012a).

Bedrock near the sampling sites has been described as granodiorite with moderate shearing (producing proto- to ultramylonites) and mafic dykes (British Antarctic Survey, 1967). The crystallisation age of the granodiorite at Mount Sullivan is 178 ± 2 Ma according to Rb—Sr whole-rock dating (Pankhurst, 1983), or 183 ± 3 Ma according to U—Pb isotopes in zircon (Riley et al., 2017). Heterogenous igneous assemblages, zoned K-feldspar, and xenoliths of gabbro in granodiorite bodies provide evidence for mingling between parent felsic and mafic melts and suggest synplutonic emplacement (Vaughan et al., 2002). Additionally, unpublished data suggests a Triassic age for an unlocated granite sample at Mount Sullivan (Vaughan et al., 2012b).

At Engel Peaks, a large, steep reverse fault demarks the eastern limit of the EPLSZ and contributes to a diverse plutonic, volcanic and metasedimentary local geology (Fig. 1; British Antarctic Survey, 1971b; Cox et al., 2023; Meneilly, 1988; Meneilly et al., 1987). The geochronology of Engel Peaks is poorly constrained although the Engel Peaks 'granite' outcropping on the easternmost flanks of the mountains is thought to be the oldest of the sequence and related to granitoid intrusions at Mount Sullivan (British Antarctic Survey, 1971b; Davies, 1984). Later maps of Engel Peaks reclassified the orthoclase and quartz-rich granite as granophyre (Meneilly, 1988) and suggest it intruded through rhyolitic and basaltic basement at ~113 Ma (Meneilly et al., 1987). However, Riley et al. (2017) described a 'sheared granitoid' here and dated it to 188 ± 1 Ma (zircon U—Pb). Immediately west, the granophyre is overlain by a ~ 1 km wide zone of ductile deformation featuring complex pseudotachylites/breccias of angular granite and mylonites. Some mylonites contain pods of undeformed granite (Meneilly, 1988). Complex sequences of mudstones, sandstones, conglomerates, slates, schists, tuffs, vesicular basalts are then superposed. Samples were taken from this complex lithological zone on the western flank of South Engel Peak.

4. Samples and methods

4.1. Sampling

Rock samples ($n = 34$) collected from Mount Faith, Mount Sullivan, and Engel Peaks in northeast Palmer Land on the Antarctic Peninsula (Fig. 1) were accessed from the BAS rock archives. Samples were collected along the northeastern ridges of Mount Faith and Mount Sullivan and the western ridge of South Engel Peak. Bedrock ($n = 14$) at all three sites is commonly frost shattered. Boulders ($n = 20$) that were sampled are assumed to be derived in situ and represent the geology at the sample coordinates, unless proven otherwise, because it is unlikely that past or present cold-based ice flow has moved boulders upwards onto ridges at these locations. Sample metadata are provided in Table 1.

4.2. Sample processing

Eleven whole-rock samples from Mount Faith and two from Mount Sullivan were used here for in situ petrology, bulk geochemistry, and to extract zircon for petrochronology. Finely crushed separates (<125 μm) were available for the other ten Mount Faith samples, seven Mount Sullivan samples, and all four Engel Peaks samples and were used to extract zircon for petrochronology. The <75 μm fraction, which was available for all samples was used to identify the mineral phases present using powder X-ray diffraction spectroscopy.

At the University of Wollongong (UOW), whole-rock samples were subsampled to create thin (30 μm) sections for optical mineralogy and polished blocks 5 × 20 × 50 mm for in situ geochemical analyses (Supplementary material 1). The remaining bulk rock samples were crushed in a jaw crusher that was pre-cleaned with a scrubber and pressurised air. Subsamples for bulk geochemical analysis (~20 g) were milled into a fine powder using a tungsten carbide TEMA ring mill that was pre-cleaned by milling pure quartz sand and air cleaning the quartz dust. The remainder of the eleven samples crushed at UOW, and the fine separates from BAS, were sieved to obtain the 63–125 μm size fraction to extract zircon.

High purity zircon separates were extracted from the 63–125 μm fraction using a density separation and 'micro-panning' method. Samples were deslimed with water and treated with a 20 % solution of HCl and MilliQ deionised water to leach Fe from mineral surfaces which can degrade lithium sodium heteropolytungstate (LST) heavy liquid. After rinsing and drying, heavy minerals were separated using LST at a density of 2.84 g cm^{-3}. Zircon crystals were isolated from 1 to 5 g of other heavy minerals by 'micro-panning' in a watch glass with water and collected with a clean pipette. Magnetic impurities were removed using a neodymium hand magnet. Crystals from zircon separates were hand-picked using a needle, mounted onto double-sided tape and set within a 25 mm diameter disc of Struers EpoFix epoxy resin. Crystal centres were exposed by grinding the face of the mount with 1200-grit sandpaper before polishing on silk pads with 1 μm and 0.3 μm diamond suspensions. Mounts were wiped clean with ethanol, then ultrasonically cleaned for 5 min with 1 M HCl and deionised water. Mounts remained uncoated for further analyses.

Table 1
Sample information.

Sample	Latitude (dd)	Longitude (dd)	Elevation (m)	Type
Mount Faith				
N.8.05	−69.630267	−64.270283	1932	Boulder
N.8.06	−69.629850	−64.270183	1923	Bedrock
N.8.08	−69.631600	−64.266600	1961	Boulder
N.8.09	−69.632800	−64.263017	1979	Boulder
N.8.11	−69.632983	−64.262650	1986	Boulder
N.8.12	−69.633183	−64.261967	1994	Boulder
N.8.13	−69.633367	−64.261217	2003	Boulder
N.8.14	−69.634083	−64.256367	2046	Bedrock
N.8.15	−69.633817	−64.257833	2033	Bedrock
N.8.17	−69.632393	−64.264625	1968	Boulder
N.8.18	−69.631583	−64.266550	1960	Boulder
N.8.19	−69.626800	−64.281700	1907	Bedrock
N.8.20	−69.625267	−64.291167	1941	Boulder
N.8.23	−69.624450	−64.292417	1948	Bedrock
N.8.27	−69.625967	−64.288650	1929	Boulder
N.8.28	−69.614850	−64.304767	2110	Bedrock
N.8.29	−69.612510	−64.307700	2146	Bedrock
N.8.30	−69.616417	−64.303517	2065	Bedrock
N.8.31	−69.610117	−64.324633	2227	Bedrock
N.8.32	−69.609367	−64.322450	2176	Boulder
N.8.36	−69.621300	−64.295417	1983	Bedrock
Mount Sullivan				
N.8.50	−69.576867	−63.706950	1664	Bedrock
N.8.51	−69.581750	−63.754933	1885	Boulder
N.8.55	−69.580850	−63.744850	1790	Bedrock
N.8.63	−69.579483	−63.732067	1689	Bedrock
N.8.65	−69.577950	−63.698033	1584	Boulder
N.8.67	−69.578033	−63.695683	1589	Bedrock
N.8.68	−69.578300	−63.691117	1586	Boulder
N.8.69	−69.578050	−63.695783	1589	Boulder
N.8.70	−69.578050	−63.695783	1589	Boulder
Engel Peaks				
N.8.83	−69.537750	−63.107433	1255	Boulder
N.8.84	−69.540183	−63.117883	1241	Boulder
N.8.85	−69.535850	−63.101817	1320	Boulder
N.8.88	−69.538000	−63.108133	1248	Boulder

4.3. Optical and scanning electron microscopy

Mineral identification and petrological observations were made of thin sections using a Leica M205A optical microscope at 4× and 10× magnification in plane-polarised and cross-polarised transmitted light. In situ geochemical observations of polished blocks were made using back-scattered electron (BSE) microscopy and semi-quantitative energy dispersive X-ray (EDX) spectroscopy using a PhenomXL benchtop scanning electron microscope (SEM) at UOW.

Zircon mounts were imaged with a Leica DM2500P optical microscope with plane-polarised transmitted (10× magnification) and reflected light (4× magnification) to identify regions of interest, topographic defects, and inclusions (Supplementary material 2). Panchromatic cathodoluminescence (CL) images were acquired within the wavelength range 230–800 nm using a Gatan MonoCL4 detector connected to the JEOL JSM-6490LV SEM at the Electron Microscopy Centre, UOW. CL images were run under high vacuum with an acceleration voltage of 15 kV, 20 nA beam current and 10–20 ms dwell time. The widest aperture (100 μm) was used to generate maximum signal intensity.

4.4. Whole-rock X-ray fluorescence (XRF) spectroscopy

The major- and trace-element composition of the thirteen whole-rock samples were determined using a Spectro Ametek XEPOS III energy-dispersive X-ray fluorescence spectrometer at UOW. Major element concentrations were measured in glass-fusion beads containing ~0.4 g of sample and ~ 4 g of lithium metaborate flux to minimise issues with sample heterogeneity and matrix effects. Trace element concentrations were measured in ~5 g of powdered sample pressed into pellets. Geological reference materials G-2 and BHVO-2 were measured alongside unknowns to assess accuracy relative to the GeoReM preferred values (Jochum et al., 2016). Major element data are plotted and discussed in text on a volatile-free basis.

4.5. Whole-rock and fine fraction X-ray diffraction (XRD) spectroscopy

Mineralogical compositions were characterised using X-Ray Diffraction (XRD) analysis on powdered whole-rock or powdered fine fraction (<63 μm) material. Powdered samples were analysed at UOW using an ARL ThermoFisher Equinox 1000 X-Ray diffractometer. This instrument uses Cu Kα radiation with an operating voltage of 40 kV and 30 mA together with a germanium monochromator. This system has an asymmetric geometry and curved detector that allows diffraction peaks to be measured simultaneously across a wide spectrum. Mineral phases were identified using Crystal Impact's *Match!* software (Version 4.1, Build 309) as well as the Crystallographic Online Database (Version 03/06/2024).

4.6. Laser ablation inductively coupled plasma mass spectrometry (LA-ICP-MS)

Zircon U—Pb and trace element analyses were conducted at the Central Analytical Research Facility (CARF), Queensland University of Technology, using an ESI/New Wave Research Coherent ExciStar XS 193 nm laser ablation system coupled to an Agilent 8900 ICP-MS. A total of 1148 spots across 30–50 grains for each one of 34 samples as well as 300 spots on four zircon reference materials and the NIST610 standard were analysed over two full-day sessions. Spot locations were chosen to avoid fractures and inclusions. For some grains with apparent growth zones visible in CL imagery, two spots were chosen to examine intra-grain variability between 'core' and 'rim'. The experiment was designed so that one analysis of the doped glass standard NIST 610 and zircon reference materials 91,500 (Wiedenbeck et al., 1995), GJ-1 (Jackson et al., 2004), Plešovice (Sláma et al., 2008), and Temora 2 (Black et al., 2004) were bracketed around 15–20 'unknowns'.

Circular spots of 25 μm diameter were ablated with a pulse rate of 7 Hz, fluence of 2.7 J cm^{-2} and dwell time of 30 s resulting in ablation to ~15–20 μm depth. Carrier gas flow to the ICP-MS was 700 ml min^{-1} of He from the cell combined with 700 ml min^{-1} of Ar make-up gas in a mixing bulb at a Y-piece. Masses collected for U—Pb dating and trace element analysis are listed with their integration time in Table 2. All analytical conditions are presented in Supplementary material 3 following reporting recommendations described by (Horstwood et al., 2016).

Data were reduced in *Iolite v4.9.4* with the aid of *VisualAge* (Paton et al., 2011; Petrus and Kamber, 2012). Spot ablations were individually checked for spurious results caused by inclusions, metamict regions, Pb anomalies or mixed age zones and adjusted or excluded if necessary (Supplementary material 3). Inclusions were identified by large spikes in Al, P, Ti or La. Metamict regions contained concentrations of U that exceeded several thousand grams-per-microgram and were very dark under in CL images. Spots with anomalous Pb counts that did not resemble parent U counts, and exhibited discordant ages, were assumed to have open system Pb behaviour and excluded. Ablation through mixed age zones, apparent by sudden and parallel changes to parent U and daughter Pb counts, were adjusted to separate data into distinct measurements if possible.

For U—Pb isotopes, Temora 2 ($^{206}Pb/^{238}U$ age = 416.8 ± 1.3 Ma; Black et al., 2004) was used as the primary external reference material. Zircon 91,500 (Wiedenbeck et al., 1995), GJ-1 (Jackson et al., 2004), and Plešovice (Sláma et al., 2008) were used as secondary reference materials and measured weighted mean ages are in good agreement with their accepted $^{206}Pb/^{238}U$ ages for both analytical sessions (Supplementary material 3). Isotope ratios were exported from *Iolite* to calculate individual ages, weighted mean ages and plot concordia graphs in *IsoplotR* (Vermeesch, 2018). Ages that were more than 10 % discordant based on the concordia distance were filtered out of weighted mean age calculations (Vermeesch, 2021), as well as concordant ages from inherited cores. No common Pb correction was applied. All errors presented are standard errors at the 2σ level.

Trace element concentrations were calculated using the new '3D Trace Elements' data reduction scheme (Paul et al., 2023) in *Iolite* which accounts for time-dependent sensitivity drift in LA-ICP-MS analyses and can use multiple reference materials. NIST610 and 91,500 were both used to create a calibration surface and ^{29}Si was used an internal standard. Ablation yields from 91,500 were normalised to NIST610 for isotopes common to both reference materials to avoid matrix effects

Table 2
Masses measured by LA-ICP-MS.

Element	Mass	Integration time (s)
Al	27	0.01
Si	29	0.005
P	31	0.01
Ti	49	0.02
Zr	91	0.003
Nb	93	0.005
La	139	0.01
Ce	140	0.01
Pr	141	0.01
Nd	146	0.01
Sm	147	0.01
Eu	153	0.01
Gd	157	0.01
Yb	172	0.01
Lu	175	0.01
Hf	177	0.005
Ta	181	0.01
Pb	206	0.035
Pb	207	0.035
Pb	208	0.035
Th	232	0.03
U	235	0.035
U	238	0.03

when creating the calibration surface. Downhole fractionation was corrected for each isotope using a linear model relative to the internal standard forced to the origin. GJ-1 was used a secondary reference material and measured concentrations were in good agreement with the accepted values (Supplementary material 3). Uncertainty is presented as standard errors at the 2σ level. Note that in Session 1, the measured [Hf] in NIST610 was ~40 % less than the expected concentration (~500 ppm), but not in 91,500, causing [Hf] in unknowns to be artificially

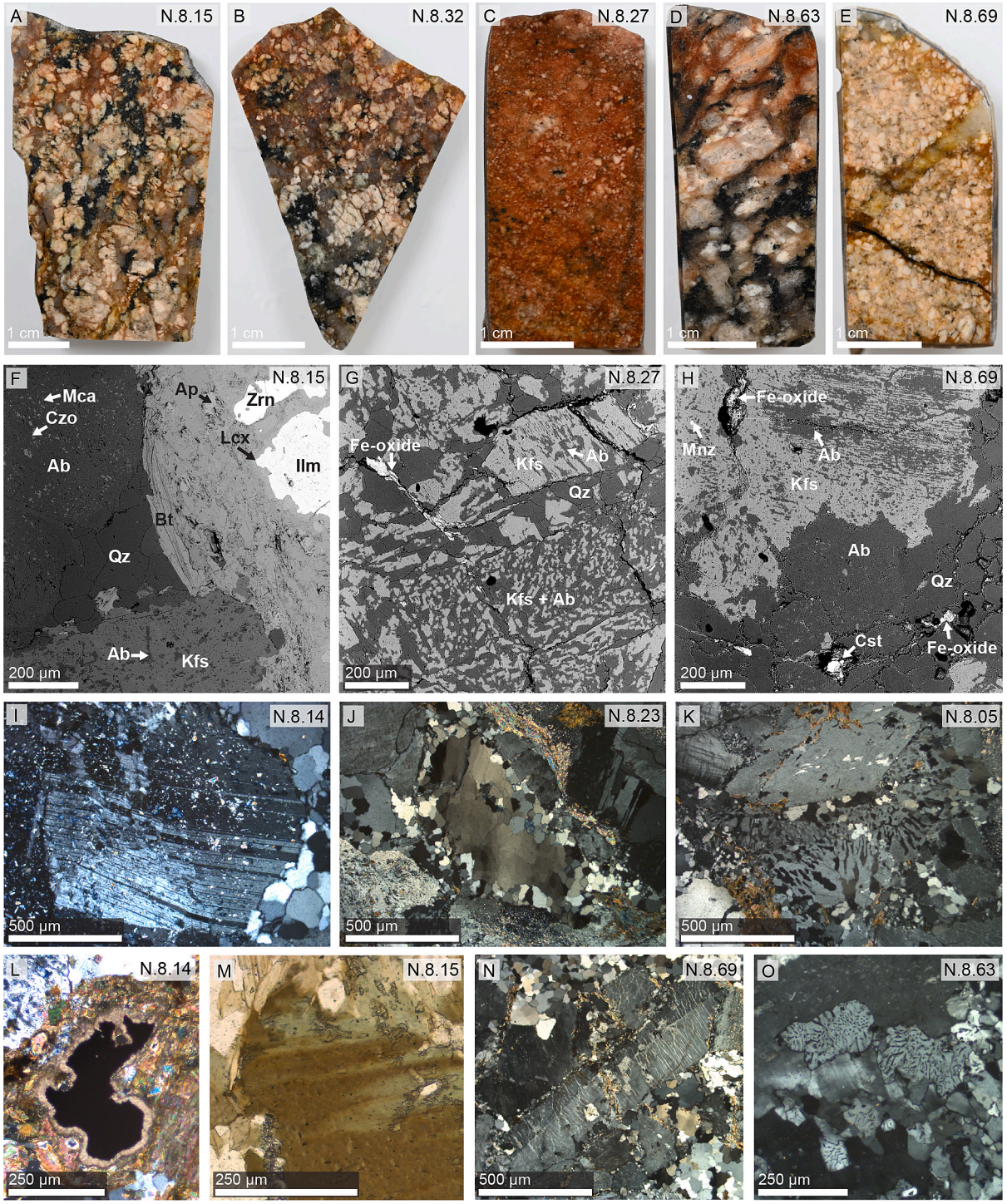

Fig. 2. (A – E) Example polished granitoid blocks from Mount Faith (A – C) and Mount Sullivan (D – E). (F – H) Example BSE images and labelled mineral phases from Mount Faith (F, G) and Mount Sullivan (H), where Ab – albite, Ab (Mca + Czo) – albite with secondary mica and clinozoisite, Ap – apatite, Bt – biotite, Cst – cassiterite, Ilm – ilmenite, Kfs – K-feldspar, Lcx – leucoxene, Mnz – monazite Ttn – titanite, Qz – quartz, Zrn – zircon. (I – M) Example thin section microphotographs of Mount Faith granitoids in cross-polarised light (I – L) and plane polarised light (M), showing: (I) brittle deformation of multiple twinning in albite and secondary alteration to sericite and clinozoisite, (J) bimodal size distribution of partially recrystallised quartz where larger grains retain undulose strain, (K) granophyric quartz and K-feldspar intergrowths, (L) leucoxene alteration coronas around ilmentite, and (M) partial replacement of biotite by chlorite. (N, O) Thin section microphotographs in cross polarised light of Mount Sullivan granitoids showing: (N) albite exsolution and brittle fracturing of K-feldspars, recrystallised quartz, and secondary mica growth, and (O) myrmekites at K-feldspar boundaries.

inflated by ~3000 ppm and therefore incomparable between sessions. Hf in zircon concentrations are presented in Supplementary material 3 but are not discussed here.

5. Results

5.1. Petrography

Nine thin section and polished block pairs from Mount Faith and two from Mount Sullivan provided petrographic observations using optical and scanning electron microscopy (Fig. 2, Supplementary material 1). Mount Faith granitoids are generally leucocratic, coarse-grained and exhibit porphyritic alkali feldspar phenocrysts with equigranular quartz and plagioclase. Mafic minerals are mostly biotite and secondary chlorite, as well as accessory apatite, titanite, zircon, and ilmenite, and sometimes cassiterite, magnetite, muscovite, monazite and/or Fe-oxides (Fig. 2a, b, f). Quartz is anhedral and partially recrystallised with an inequigranular, bimodal size distribution (~100 μm and 1–2 mm diameter). Larger quartz persists with visible strain (undulose extinction in cross-polarised light). Alkali feldspar crystals are subhedral to anhedral, 2–10 mm (mostly 5 mm) and perthitic. Subhedral to anhedral plagioclase crystals (1–2 mm) are alteration to sericite and epidote group minerals such as clinozoisite (Fig. 2i). Individual platy biotite crystals (100–300 μm) occur in elongated clots 3–6 mm long with accessory minerals. Feldspars have brittle fractures infilled with quartz. Often chlorite has partially or completely replaced biotite and ilmenite crystals have irregular, rounded boundaries and feature coronas of leucoxene (Fig. 2l–m).

Some Mount Faith granitoids have unique features. N.8.11 and N.8.32 contain both ilmenite and magnetite, whereas in other samples magnetite was not observed in thin sections or polished blocks. N.8.5 and N.8.36 exhibit granophyric quartz and alkali feldspar intergrowths (Fig. 2k). N.8.11, N.8.32 and N.8.36 host cassiterite within quartz and plagioclase. N.8.27 differs from the other samples at Mount Faith because it is composed of reddish-brown, fine-medium grained (~1 mm) equigranular quartz and alkali feldspar, but not plagioclase (Fig. 2c). Quartz is partially recrystallised and exhibits undulose extinction. Alkali feldspar crystals feature exsolution textures of albite and minor sericitic alteration. Granophyric quartz and feldspar are present as well as limited accessory zircon, Fe-oxides, and rare orthopyroxene. Secondary hematite is present between grain boundaries of N.8.27. For samples without whole-rock available, XRD analyses indicate major mineralogy consisting of quartz, orthoclase, albite, biotite and accessory muscovite.

Thin sections and polished blocks of N.8.63 and N.8.69 from Mount Sullivan are leucocratic, medium- to coarse-grained granitoids and exhibit features of deformation and alteration (Fig. 2, Supplementary material 1). N.8.63 is porphyritic with large (2–8 mm) subhedral to euhedral alkali feldspar in a groundmass of 2–4 mm subhedral to euhedral plagioclase and two size classes (~50 μm and 0.2–1 mm) of recrystallised quartz (Fig. 2d, o). Elongate clumps of mafic and accessory minerals such as biotite, chlorite, muscovite, magnetite, ilmenite, cassiterite, and zircon are associated with the smaller recrystallised quartz. Some alkali feldspar phenocrysts exhibit vermicular exsolution textures. Occasional myrmekites adjoin alkali feldspar phenocrysts. Some plagioclase crystals are brittlely fractured and feature secondary epidote group minerals such as clinozoisite.

N.8.69 is a leucocratic granitoid with equigranular quartz, albite and alkali feldspar of medium (~1–2 mm) size and minor interstitial accessory minerals (Fig. 2e, h). Quartz is partially to fully recrystallised and remaining larger grains have undulose extinction. Alkali feldspar exhibits vermicular exsolution textures, and evidence for brittle fracturing is visible in both feldspars (Fig. 2n). Muscovite is present between grains and as an alteration product of feldspars. Fe-oxides and cassiterite are present as interstitial blobs. Other accessory minerals include zircon, monazite, and rutile. One 2–4 mm wide cross-cutting quartz vein is associated with Fe-oxides and pyrite which is partially oxidised to Fe-oxide.

Crushed samples from Mount Sullivan are composed of quartz, albite, orthoclase, biotite and muscovite according to XRD spectra. Samples N.8.50, N.8.51, N.8.55 and N.8.70 are dominated by quartz, albite, and muscovite. Crushed samples from Engel Peaks are composed of the same five major constituents, although N.8.84 and N.8.88 do not contain significant amounts of either mica.

5.2. Whole-rock geochemistry and mineralogy

Major and trace element data for eleven whole-rock samples from Mount Faith and two from Mount Sullivan are presented in Table 3. Volatiles lost on ignition account for 0.8–1.2 wt% in all samples. Mount Faith samples are granites (sensu stricto) based on a volatile-free Total Alkali-Silica classification, except for N.8.11 which is a granodiorite (Fig. 3a). Mount Faith granites have enriched SiO_2 and K_2O, and depleted CaO, Na_2O, and MgO relative to average upper continental crust (Taylor and McLennan, 1985). They are ferroan, peraluminous and calc-alkaline volcanic arc granites (Fig. 3b-e). The granodiorite from Mount Faith (N.8.11) is poor in SiO_2 and K_2O, and rich in Al_2O_3, making it strongly peraluminous relative to other samples from Mount Faith. N.8.32 is depleted in Fe_2O_3, MgO, and CaO, and enriched in SiO_2 compared to adjacent granites. The two samples (N.8.63, N.8.69) from Mount Sullivan have a volatile-free geochemical makeup like a granite (Fig. 3a). Volatiles account for 0.5–0.6 wt% (Table 3). Both samples are enriched in SiO_2 and K_2O, and moderately to strongly depleted in Fe_2O_3, TiO_2, MgO, and CaO relative to upper continental crust (Taylor and McLennan, 1985). Both samples are ferroan, peraluminous and calcic to calc-alkaline in composition with a volcanic arc signature (Fig. 3b-e). Note that granitoids at Mount Faith and Mount Sullivan may be affected by post-emplacement alteration that would induce scatter within whole-rock geochemical indices. However, we assume that the general grouping of the indices remains accurate to the original geochemical and tectonic classifications.

5.3. Zircon petrology

Mount Faith zircon crystals are typically euhedral, doubly-terminated prisms, 30–200 μm (average ~ 100 μm) and have a width to length ratio 1:2–1:3. They are transparent and colourless, and inclusions are common. Some crystals from N.8.30 are subhedral to rounded and often fractured, and some from N.8.36 are translucent and champagne coloured. Mount Sullivan zircon crystals are subhedral to euhedral, doubly-terminated prisms, translucent to transparent, colourless to champagne and 40–160 μm in size with a 1:2–1:3 width to length ratio. Inclusions are frequent, except in N.8.67 (Supplementary material 2). Zircon crystals from Engel Peaks are subhedral to euhedral, terminated prisms, 50–200 μm (average ~ 100 μm) and have a width to length ratio of 1:2–1:3. They are transparent and colourless to champagne coloured. Grains in N.8.83 and N.8.85 show irregular iron staining. Most have inclusions and fractures.

CL images reveal that all zircon crystals from Mount Faith feature oscillatory zoning from the centre to edge, or within a mantle that surrounds a core of a different pattern (Fig. 4, Supplementary material 2). Cores are often very dark in CL, with sub-rounded to rounded boundaries and feature wider-scale oscillatory zones and sector zoning. Some crystals feature thin, almost non-luminescent rims. Many crystals feature rounded, non-luminescent inclusions. Mount Sullivan zircon crystals display similar patterns in CL images. They differ by having some dark ‘cores’ that constitute almost the entire crystal with only a thin oscillatory zoned rim. Some cores of Mount Sullivan zircon have brighter CL emissions and reveal disrupted zones. Zircon crystals from Engel Peaks can range from completely dark in CL to a typical oscillatory or sector zoned structure. One crystal from N.8.84 is subrounded and exhibits bright CL inside a thin dark CL rim. Zircon from N.8.88 are mostly dark but some oscillatory and complex zoning can be resolved.

Table 3
Whole-rock XRF geochemistry.

Sample (N.8.XX)	Mount Faith											Mount Sullivan	
	05	09	11	12	13	14	15	23	29	32	36	63	69
Major element oxides (wt%)													
SiO_2	71.31	72.68	67.49	70.33	71.96	71.32	72.47	70.85	71.09	74.11	72.09	76.00	78.05
TiO_2	0.48	0.49	0.45	0.49	0.45	0.47	0.48	0.49	0.49	0.35	0.46	0.21	0.08
Al_2O_3	13.59	13.15	19.35	15.26	14.22	13.34	12.96	13.81	13.53	13.60	13.24	11.83	12.31
Fe_2O_3	3.34	3.42	2.90	3.05	3.07	3.55	3.35	3.23	3.54	2.36	3.24	2.34	0.78
MnO	0.05	0.07	0.03	0.04	0.05	0.05	0.05	0.03	0.04	0.03	0.03	0.04	0.01
MgO	0.44	0.56	0.44	0.46	0.42	0.49	0.48	0.49	0.49	0.18	0.46	0.13	< 0.01
CaO	2.03	1.20	2.33	2.08	1.76	2.03	1.94	2.09	1.47	0.72	1.86	1.24	0.17
Na_2O	2.58	2.66	3.20	2.98	2.25	2.73	2.72	3.09	2.96	3.40	2.68	2.54	2.62
K_2O	4.82	4.56	2.53	3.94	4.67	4.47	4.45	4.68	4.82	4.04	4.70	4.94	5.10
P_2O_5	0.31	0.11	0.10	0.10	0.09	0.09	0.09	0.09	0.09	0.09	0.09	0.03	0.05
SO_3	0.06	0.02	0.08	0.03	0.01	0.11	0.01	0.02	0.06	0.06	0.01	0.04	0.03
LOI	*0.78*	*0.85*	*0.95*	*1.03*	*0.86*	1.15	0.81	0.91	1.01	0.88	0.94	0.51	0.62
Total	93.82	94.24	96.19	94.68	94.17	99.79	99.80	99.77	99.58	94.75	99.79	99.85	94.03
Trace elements (ppm)													
Cl	127.1	90.1	62.2	75.6	63.6	121.5	107.4	150.6	156.7	71.2	182.2	80.2	55.1
V	41.6	39.2	39.5	40.7	42.2	37.0	49.9	45.8	40.2	30.9	46.9	17.2	< 1.0
Cr	11.2	8.9	9.3	9	18.8	108.1	98.6	137.8	94.9	7.4	111.0	157.3	4.2
Co	46.8	48	55.7	52.6	52.6	14.8	14.8	13.6	12.2	57.6	13.5	12.9	60.5
Ni	5.9	10.6	5.6	13.3	5.9	7.7	12.3	8.2	9.2	6.1	11.9	8.1	5
Cu	8.6	8.6	7.4	9	5.3	11.9	5.8	3.9	5.7	5.2	6.4	5.3	3.9
Zn	39.7	53.4	23.5	32.1	50.7	44.8	41.8	22.2	36.1	19.9	22.8	31.6	19.7
Ga	15.4	14.7	15.8	15.3	15.6	14.8	14.3	15.0	16.0	15.5	14.3	12.4	14.8
Ge	< 0.1	< 0.5	< 0.5	1.3	< 0.4	1.6	2.2	2.2	2.3	< 0.5	1.4	1.7	< 0.5
As	1.2	1.6	2.3	1.6	1.9	1.8	1.3	2.5	2.5	2.4	3.7	0.3	3.7
Se	0.8	0.8	1.1	0.9	0.9	0.4	0.1	0.2	0.3	1.3	0.1	0.3	1.1
Br	< 0.5	< 0.5	< 0.5	< 0.5	< 0.5	< 0.5	< 0.5	0.5	0.5	< 0.5	0.6	< 0.5	< 0.5
Rb	199.6	154.2	99.8	100	170	193.7	195.6	198.8	200.6	144.8	201.7	184.1	174.2
Sr	139.9	102.5	145.1	137.6	148.6	150.4	145.2	144.3	152.3	101.2	143.1	56.2	83.2
Y	30.9	34.1	30.1	34.2	29.3	28.5	30.0	30.5	27.5	29.4	31.4	28.1	39.1
Zr	192.2	251.3	202.8	242.6	197.7	207.3	237.5	226.3	232.0	260.9	219.3	182.8	100.5
Nb	12.2	13	12.1	12.4	11.1	12.8	11.9	13.3	12.3	12.8	12.7	13.2	9.8
Cd	< 2.0	< 2.0	< 2.0	< 2.0	< 2.0	< 2.0	0.8	< 2.0	< 2.0	< 2.0	< 2.0	< 2.0	< 2.0
Sn	1.5	6.2	4.5	3	4.7	7.0	4.9	8.4	8.5	9.6	< 3.0	1.3	6.3
Sb	< 3.0	< 3.0	< 3.0	< 3.0	< 3.0	< 3.0	< 3.0	< 3.0	< 3.0	< 3.0	< 3.0	< 3.0	< 3.0
Cs	< 4.0	< 4.0	< 4.0	< 4.0	< 4.0	< 4.0	< 4.0	< 4.0	< 4.0	< 4.0	< 4.0	< 4.0	< 4.0
Ba	866.5	1120	968.3	1152	876.8	756.6	829.5	758.5	894.1	1112	802.8	669.5	208.2
La	66.5	62	53.6	53.5	85	55.6	50.1	39.4	58.9	42	47.9	58.8	51.8
Hf	4	4.8	4	5	3.5	3.3	4.7	5.3	3.5	4.9	4.0	3.2	4.1
Ta	2	6.5	2.8	1.6	2	2.6	2.2	2.7	1.4	4.4	2.2	2.5	4.4
W	342.8	331.8	414.1	379.1	379.1	< 1.0	< 1.0	< 1.0	< 1.0	535.4	< 1.0	< 1.0	436.4
Pb	20.9	24.8	12.4	16.7	34.7	22.2	19.8	16.9	24.1	13	16.9	18.8	64.1
Th	16.9	20.8	15.6	19.3	11	17.7	16.2	17.3	15.9	19.4	19.6	21.7	22.1
U	6	3.7	3.5	3.7	1.6	2.2	2.5	2.4	1.7	2.8	4.3	3.0	1.9

5.4. Zircon U—Pb isotope geochronology

A total of 767 spots on zircon crystals from 21 samples from Mount Faith, 292 spots in nine samples from Mount Sullivan, and 87 spots in four samples from Engel Peaks were analysed for U—Pb isotopes. Some analyses were discordant or otherwise spurious and were excluded from the summary of results below. Weighted mean ages are reported in Table 4 and plotted in Fig. 5 alongside a representative Tera-Wasserburg concordia diagram from each site. All spot results are presented in Supplementary material 3 and all U—Pb concordia and weighted mean age plots are presented in Supplementary material 4. Weighted mean ages are calculated for spots representative of the magmatic age, where appropriate, and excludes spots from inherited cores.

5.5. Mount Faith

The range of $^{206}Pb/^{238}U$ ages from individual spots ($n = 574$) from all samples range from 161.7 ± 7.5 to 1709 ± 53 Ma. In samples from Mount Faith (excluding N.8.8, N.8.11, and N.8.18), 50 individual spots were identified as inherited cores or older grains and comprised ages 194.0–1709 Ma. Weighted mean ages representative of the magmatic age ranged between 180.6 ± 1.4 Ma (MSWD = 2.2) and 188.9 ± 1.2 Ma (MSWD = 1.1) for the 21 samples at Mount Faith (Table 4). This range excludes a less robust weighted mean age of 179.2 ± 3.1 Ma (MSWD = 15) from N.8.27 with high uncertainties inherited from 5 of 22 spot analyses being concordant.

5.6. Mount Sullivan

Individual $^{206}Pb/^{238}U$ spot ages ($n = 238$) from samples at Mount Sullivan ranged between 106.8 ± 3.7 Ma and 784 ± 29 Ma. Excluding 21 inherited cores, most samples exhibit similar populations where spot ages range between 170.6 ± 6.5 Ma and 196.9 ± 12.8 Ma ($n = 167$), and weighted mean ages are 183.6 ± 1.0 Ma (MSWD = 3) to 187.7 ± 1.7 Ma (MSWD = 1.3). Note, only five zircon crystals were recovered from N.8.69 but were all concordant and in good agreement (186.0 ± 3.0, MSWD = 0.72).

Zircon populations in N.8.51 and N.8.70 from Mount Sullivan differ from the rest. Zircon from N.8.51 exhibited ages between 106.8 ± 3.7 Ma and 266.6 ± 11.5 Ma ($n = 30$) with most results clustered around ~120 Ma, a secondary age cluster at ~180 Ma, and a tertiary cluster at ~150 Ma (Fig. 5f). The weighted mean age of the youngest cluster, assumed here to represent the magmatic age, is 115.6 ± 1.0 Ma (MSWD = 5.6, $n = 18$). The ~150 Ma cluster (n = 3) likely represents sampling

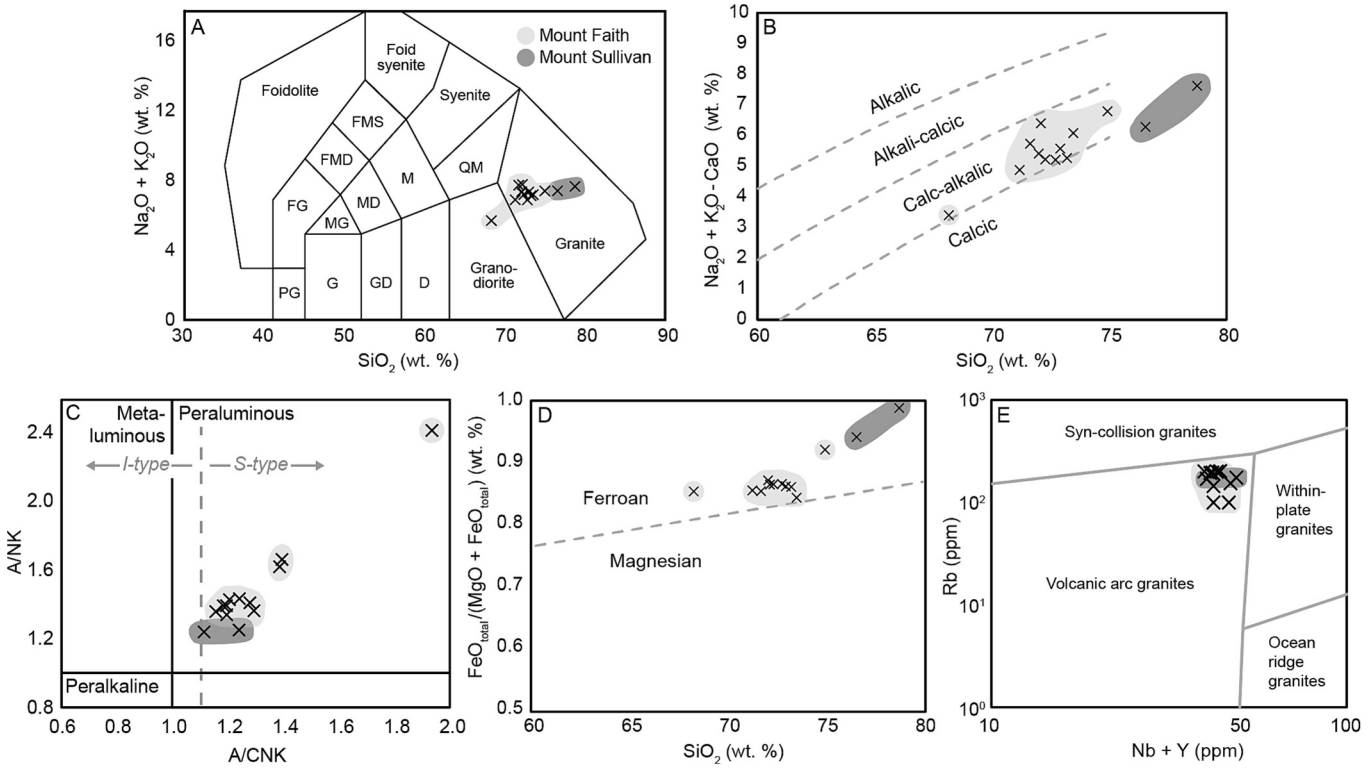

Fig. 3. Whole-rock geochemistry classification schemes for Mount Faith and Mount Sullivan granitoids: (A) Total Alkali-Silica plutonic rock classification diagram (Middlemost, 1994) where D = diorite, G = gabbro, GD = gabbroic diorite, FG = foid gabbro, FMD = foid monzodiorite, FMS = foid monzosyenite, M = monzonite, MD = monzodiorite, MG = monzogabbro, PG = peridot gabbro, and QM = quartz monzonite, (B) Modified Alkali-Lime Index (Frost et al., 2001), (C) Aluminium Saturation Index (Frost et al., 2001) and I- or S-type classification (Chappell and White, 1992), (D) Fe-index (Frost et al., 2001), and (E) Rb vs. Nb + Y tectonic discrimination for granitic rocks (Pearce et al., 1984).

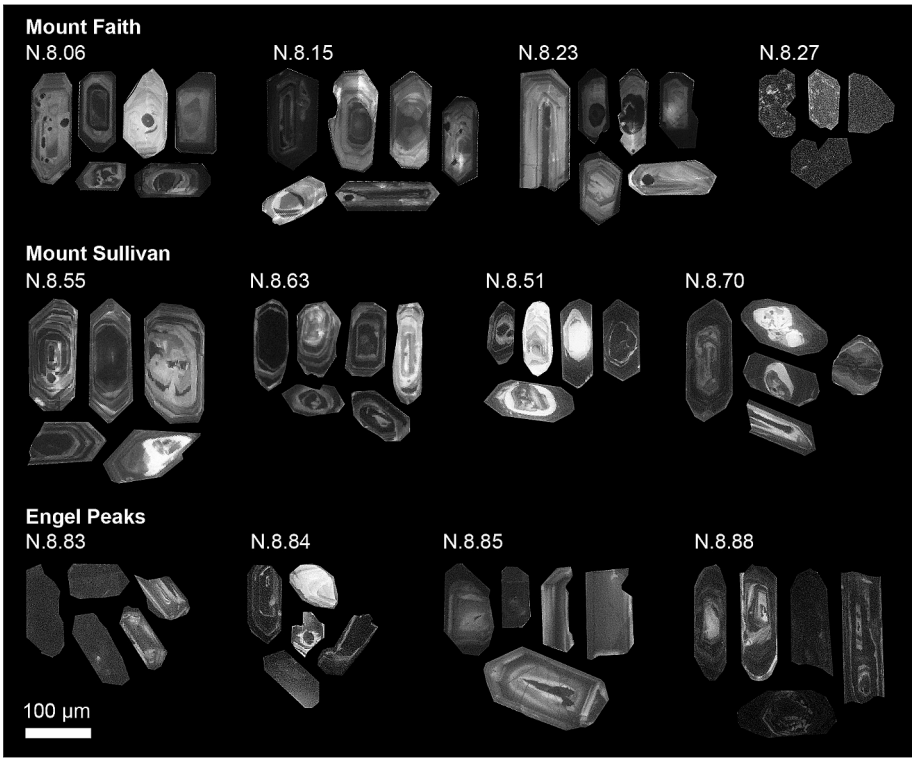

Fig. 4. Example CL images of zircon crystals from Mount Faith, Mount Sullivan and Engel Peaks. Samples typically feature oscillatory zoning, distinct cores or thin rims that can exhibit non-luminescent or very bright CL, complex zoning, and non-luminescent inclusions. N.8.27 from Mount Faith and is essentially non-luminescent. Zircon from Engel Peaks exhibit dark CL more often than the other sites.

Table 4
Weighted mean $^{206}Pb/^{238}U$ crystallisation age of samples.

Sample	Analysis session	Weighted mean age (Ma)	2σ (Ma)	n =	MSWD
Mount Faith					
N.8.05	1	182.5	1.4	21	1.2
N.8.06	1	180.6	1.1	34	1.6
N.8.08	1	184.3	2.2	10	0.54
N.8.09	1	188.5	1.5	21	1.2
N.8.11	1	185.6	1.7	17	1.6
N.8.12	1	182.3	1.4	23	0.88
N.8.13	1	182.5	1.3	25	1.8
N.8.14	1	183.4	1.1	40	1.0
N.8.15	1	183.4	1.2	37	1.6
N.8.17	1	188.0	1.5	19	0.42
N.8.18	1	185.2	1.3	26	0.89
N.8.19	1	180.6	1.4	22	2.2
N.8.20	1	183.0	1.7	18	0.42
N.8.23	2	181.9	1.2	30	1.1
N.8.27	2	179.2	3.1	5	15
N.8.28	2	187.4	1.5	19	1.5
N.8.29	2	188.9	1.2	34	1.1
N.8.30	2	183.8	1.4	22	1.9
N.8.31	2	185.7	1.4	22	0.74
N.8.32	2	184.5	1.2	31	0.81
N.8.36	2	184.9	1.1	40	1.0
Mount Sullivan					
N.8.50	2	184.1	1.1	28	1.6
N.8.51	2	115.6	1.0	18	5.6
N.8.55	2	183.6	1.0	36	3.0
N.8.63	2	184.4	1.1	35	3.5
N.8.65	2	187.7	1.7	18	1.3
N.8.67	2	187.3	1.4	20	0.89
N.8.68	2	184.1	1.6	18	0.63
N.8.69	2	186	3	5	0.72
N.8.70	2	120.5	1.2	11	5.1
Engel Peaks					
N.8.83	2	181.5	1.5	17	1.0
N.8.84	2	184.3	2.6	5	2.1
N.8.85	2	184.8	1.5	18	0.5
N.8.88	2	184.4	4.1	2	2.2

of mixed ~184 Ma and ~ 116 Ma ages where the spot overlaps distinct CL zones. The zircon population from N.8.70 is alike N.8.51 with individual concordant spot ages ranging between 116.3 ± 3.7 Ma and 508 ± 16 Ma ($n = 19$) with primary and secondary clusters at ~120 Ma and ~ 182 Ma, respectively (Fig. 5e). The weighted mean age of the younger cluster assumed to represent the crystallisation age is 120.5 ± 1.2 Ma (MSWD = 5.1, $n = 11$).

5.7. Engel Peaks

Samples N.8.83, N.8.84 and N.8.85 from Engel Peaks have similar zircon populations to each other and to those at Mount Faith and Mount Sullivan, where all concordant $^{206}Pb/^{238}U$ spot ages ($n = 40$) fall between 176.6 ± 5.9 Ma and 190.6 ± 6.0 Ma plus a single inherited core 1023 ± 34 Ma in N.8.84. Weighted mean ages of these three samples are 181.5 ± 1.5 Ma (MSWD = 1.0), 184.3 ± 2.6 Ma (MSWD = 2.1) and 184.8 ± 1.5 Ma (MSWD = 0.5), respectively (Table 4). The weighted mean age of N.8.84 is less robust than other samples given the small number of crystals recovered from the sample, however, the age is still valid because most spot analyses provided concordant ages that are in good agreement with surrounding samples. Individual concordant $^{206}Pb/^{238}U$ spot ages ($n = 25$) on zircon from N.8.88 are distributed almost uniformly between 181.3 ± 5.9 Ma and 497 ± 16 Ma with no clustering of ages (Supplementary material 4). The youngest age of N.8.88 coincides almost exactly with the crystallisation age of N.8.83 (181.5 ± 1.5 Ma) which was sampled directly adjacent. The two youngest ages (181–187) arise from two zircon crystals dark and non-distinct in CL but have a stubbier shape and more angular edges than other crystals analysed (Supplementary material 2). The youngest crystallisation ages are also similar to the age of other magmatic samples at Engel Peaks (~184 Ma), Mount Faith (179–189 Ma) and Mount Sullivan (184–188 Ma).

5.8. Zircon trace element indices of magma evolution

The same subset of spot analyses that were used for U—Pb geochronology, where discordant and spurious measurements were filtered out, are considered valid for trace element analyses. Results are summarised below for trace elements used in key indices of magma evolution (Fig. 6, Table 5). All trace element concentrations for individual spots and summary statistics for each sample are presented in Supplementary materials 3 and 4. Crystallisation temperatures were calculated for each sample using the median [Ti] in zircon assuming TiO_2 and SiO_2 saturation given the presence of free titanite and quartz (Watson et al., 2006). Europium anomalies (Eu/Eu*) were calculated by normalising [Eu] to the geometric mean of the concentration of neighbouring trivalent elements Gd and Sm, and then normalising to chondrite values of Eu, Gd and Sm (McDonough and Sun, 1995; Trail et al., 2012). Oxygen fugacity is calculated using Ce-U-Ti systematics using sample median [Ce], [Ti] and back-calculated initial [U] (Loucks et al., 2020). Oxygen fugacity is reported relative to the fayalite-magnetite-quartz oxygen buffer (i.e., ΔFMQ), or as absolute fO_2, and is expressed in log units with a standard error of ±0.6. Absolute fO_2 are calculated using the Ti-in-zircon temperature (Loucks et al., 2020).

5.9. Mount Faith

Individual analyses on zircon from Mount Faith exhibit [U] between 136 and 19,770 ppm, [Th] between 41 and 13,985 ppm, [P] between 151 and 4789 ppm, [Ti] between 3 and 533 ppm and [Ce] between 2 and 297 ppm. Extremely high [U] and [Th], and most high [P], [Ti], and [Ce], come from zircon in N.8.27. Otherwise, 95 % of [U], [Th], [P], [Ti] and [Ce] are less than 1650 ppm, 1290 ppm, 1300 ppm, 80 ppm and 78 ppm, respectively. Inherited cores and magmatic-age zones in zircon show similar trace element concentrations in most samples, although cores of N.8.13, N.8.19, and N.8.20 are notably enriched in the aforementioned elements. Occasional cores are also enriched in some but not all trace elements; Ce is particularly variable in inherited cores. Median trace element concentrations in magmatic-age zones do not vary substantially between samples at Mount Faith, except for N.8.27. Relative to the other samples at Mount Faith, N.8.36 has lower [U] and [Th], and both N.8.31 and N.8.32 have lower [Ti]. Some samples (N.8.15, N.8.19, N.8.23, N.8.27 and N.8.28) have a large range of [Ti] that spans three orders of magnitude. Median [P] surround ~600 ppm which weakly aligns with S-type granite host rock, except the strongly enriched N.8.27 (Fig. 6, Table 5). Typical Th/U ratios were around ~0.6 but the full range was between 0.03 and 1.35, except one particularly Th-rich core in a zircon from N.8.36 with a Th/U of 2.65. Ratios of Th/U in older inherited cores were typically lower (lowest sample median 0.14) and more variable than magmatic-age zones (all sample medians >0.5). Between samples, Th/U ratios were similar for magmatic-age zones except for N.8.31 with a higher median Th/U of 0.75. The Ti-in-zircon geothermometer indicates the average zircon from Mount Faith crystallised at around ~780 °C, although variation between samples is inherited from the range of [Ti]. Eu/Eu* anomalies are very low (~0.06) for all Mount Faith samples. Using the Ce-U-Ti magma oxybarometer, the median ΔFMQ of each sample surround zero. Most samples exhibit slightly negative ΔFMQ where the lowest median is −1.2 (N.8.27). Few samples have positive median ΔFMQ (i.e., N.8.9, N.8.12, N.8.31 and N.8.32) where the highest median is +0.6 (N.8.31). Median absolute log (fO_2) is similar between all samples (around −15.3).

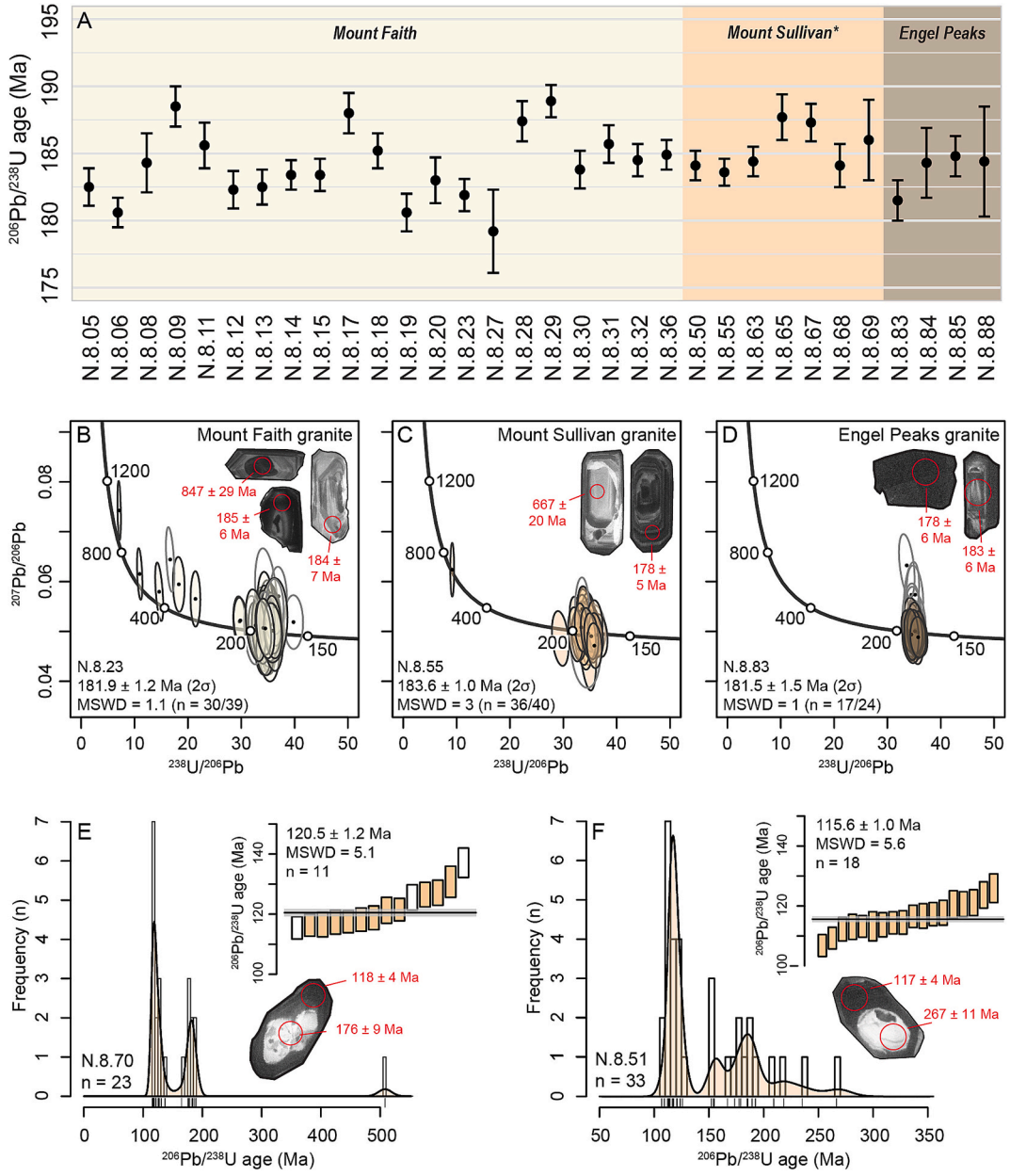

Fig. 5. Summary zircon U—Pb age results. (A) Weighted mean $^{206}Pb/^{238}U$ ages for each Early Jurassic sample from Mount Faith, Mount Sullivan, and Engel Peaks. *Denotes that Early Cretaceous ages for N.8.51 and N.8.70 from Mount Sullivan are excluded from this plot. (B – D) Tera-Wasserburg concordia plots for representative samples from each site with the interpreted magmatic weighted mean age labelled in the bottom left and example spot results overlying CL images of zircon in top right. (E, F) Kernel density estimate plots overlaid on spot age distribution histograms for Early Cretaceous recrystallised zircon. Top right shows weighted mean $^{206}Pb/^{238}U$ age plots of Early Cretaceous age zircon, and bottom right shows an example of bright CL zircon with a dark CL recrystallisation rim.

5.10. Mount Sullivan

Spot analyses from zircon from Mount Sullivan exhibit [U] between 98 and 11,420 ppm, [Th] between 54 and 26,138 ppm, [P] between 66 and 3046 ppm, [Ti] between 3 and 305 ppm and [Ce] between 2 and 355 ppm (with one outlier 1297 ppm, N.8.70 spot 19). Multiple spots have very high [U], and spots 19 in N.8.70 and 48 in N.8.63 host extremely high [Th]. Only 5 % of concentration values for U, Th, P, Ti and Ce are above 4940 ppm, 3320 ppm, 2260 ppm, 164 ppm and 100 ppm, respectively. In general, trace elements are more enriched in Mount Sullivan zircon than Mount Faith zircon. Differences between trace element concentrations in magmatic-age zones and older inherited cores are variable and sample specific. For example, inherited zircon cores in N.8.67 are enriched in U, Ti and Ce, but magmatic-age zones in N.8.63 zircon host greater trace element abundances than from cores in that sample. Spot 8c in N.8.68 hosts outstanding [P] of 7174 ppm. Early Cretaceous zircon from samples N.8.51 and N.8.70 generally host more U than older zircon in the same samples, but show no distinct difference in Th, P, Ti or Ce.

In some zircon from Mount Sullivan, [P] are around ~500 ppm which is between typical values for endmembers on the I- and S-type granite spectrum. N.8.67 and N.8.68 host greater median amounts of P (1434 ppm and 1464 ppm, respectively), and Early Cretaceous zircon from N.8.51 and N.8.70 have low [P] around ~250 ppm (Fig. 6, Table 5). Th/U ratios from all spots range from 0.07 to 2.51 and are typically magmatic, though the same P outliers have weak (N.8.67, N.8.68) to strong (N.8.51, N.8.70) metamorphic signatures (Fig. 6, Table 5). Ratios of Th/U are ~0.2 units higher in magmatic-age zones

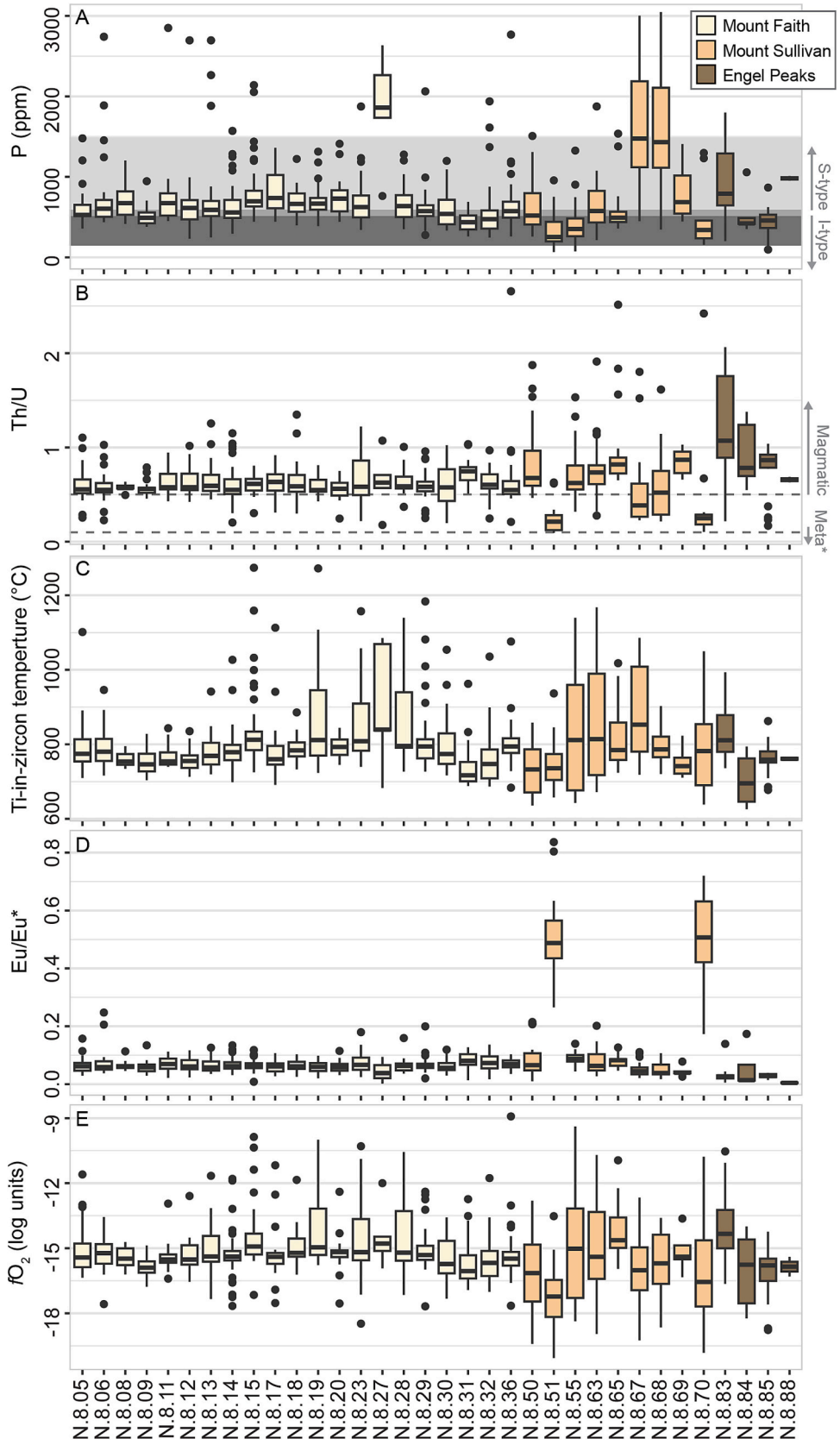

(caption on next page)

Fig. 6. Boxplots of key trace element indices in magmatic age zircon showing the range and median of individual spot results. (A) Concentration of P in zircon indicating host rock is weakly S-type for most samples, except few I-type likeness in Mount Sullivan (Burnham and Berry, 2017), (B) Th/U ratio classifying zircon as typically magmatic except for N.8.51 and N.8.70 which exhibit metamorphic recrystallisation (Kirkland et al., 2015; Yakymchuk et al., 2018). 'Meta*' is short for metamorphic. (C) Ti-in-zircon geothermometry showing typical granitic zircon crystallisation temperatures (Watson et al., 2006), (D) Eu/Eu* index suggesting strong Eu depletion in most samples but different parent melt conditions for N.8.51 and N.8.70 zircon (Trail et al., 2012; Yakymchuk et al., 2023), and (E) Absolute oxygen fugacity calculated using the Ce-U-Ti oxybarometer and Ti-in-zircon geothermometer (Loucks et al., 2020; Watson et al., 2006) showing more reduced conditions for crystallisation of N.8.51 and N.8.70. High variation within samples are inherited from high variation in [Ti].

Table 5
Median concentration of key trace elements and Th/U ratios in magmatic age zircon, as well as temperature and oxygen fugacity indices calculated from sample median.

Sample	n =	U (ppm)	Th (ppm)	P (ppm)	Ti (ppm)	Ce (ppm)	Eu (ppm)	Th/U	Ti-in-zircon temp. (°C)	Eu/Eu*	ΔFMQ (log units)	fO_2 (log units)
Mount Faith												
N.8.05	21	503	363	526	14.5	24.9	0.32	0.55	775	0.067	0.1	−15.2
N.8.06	34	547	301	605	15.4	25.8	0.33	0.55	780	0.066	0.1	−15.1
N.8.08	10	494	309	674	11.6	25.7	0.32	0.57	754	0.060	0.4	−15.4
N.8.09	21	465	265	492	10.6	19.9	0.22	0.56	746	0.056	0.1	−15.9
N.8.11	17	590	381	674	11.6	20.4	0.35	0.58	754	0.061	−0.2	−16.0
N.8.12	23	533	323	613	11.7	24.0	0.32	0.58	755	0.064	0.1	−15.6
N.8.13	26	540	320	590	13.7	23.3	0.30	0.59	769	0.053	0.0	−15.5
N.8.14	41	539	300	557	15.2	22.4	0.31	0.55	779	0.061	−0.2	−15.4
N.8.15	37	583	376	697	21.4	24.5	0.38	0.61	812	0.062	−0.4	−14.9
N.8.17	20	778	562	738	12.4	33.1	0.42	0.63	760	0.060	0.4	−15.3
N.8.18	27	659	389	665	16.0	25.2	0.32	0.59	784	0.053	−0.2	−15.3
N.8.19	22	642	352	667	21.3	27.6	0.36	0.55	812	0.062	−0.3	−14.7
N.8.20	18	469	285	730	17.7	22.3	0.35	0.56	794	0.057	−0.2	−15.1
N.8.23	32	476	281	625	20.6	20.4	0.39	0.58	808	0.061	−0.5	−15.1
N.8.27	5	12,923	8987	1861	27.9	107.9	0.23	0.63	840	0.024	−0.7	−14.6
N.8.28	19	466	298	637	18.0	22.9	0.31	0.59	795	0.045	−0.2	−15.0
N.8.29	37	398	217	575	17.9	19.2	0.27	0.58	795	0.065	−0.3	−15.2
N.8.30	23	586	303	539	14.4	19.2	0.28	0.58	774	0.055	−0.5	−15.8
N.8.31	23	581	414	437	7.6	27.2	0.74	0.75	717	0.068	0.7	−16.0
N.8.32	31	507	326	475	10.7	23.5	0.49	0.60	747	0.079	0.3	−15.7
N.8.36	40	274	150	573	17.9	13.9	0.27	0.55	795	0.077	−0.6	−15.4
Mount Sullivan												
N.8.50	29	1329	1106	519	9.1	29.1	0.31	0.68	733	0.046	−0.1	−16.4
N.8.51	18	2078	305	253	9.5	22.1	1.55	0.21	736	0.462	−1.0	−17.2
N.8.55	36	1175	741	352	22.1	28.5	0.30	0.62	816	0.086	−0.8	−15.2
N.8.63	35	1375	711	575	21.7	32.7	0.50	0.73	814	0.067	−0.6	−15.1
N.8.65	18	594	461	493	16.2	36.4	0.46	0.82	785	0.081	0.5	−14.5
N.8.67	24	699	330	1475	31.6	9.5	0.25	0.39	853	0.041	−2.5	−16.2
N.8.68	20	1197	737	1431	16.5	28.3	0.36	0.52	787	0.045	−0.5	−15.6
N.8.69	5	1827	1879	686	10.1	65.3	0.63	0.87	742	0.060	1.0	−15.1
N.8.70	12	3042	625	341	15.8	25.1	1.70	0.25	782	0.418	−1.5	−16.6
Engel Peaks												
N.8.83	17	2557	2691	792	21.1	75.5	0.59	1.07	811	0.021	0.3	−14.2
N.8.84	5	1324	923	422	5.8	49.3	0.50	0.78	695	0.022	1.2	−16.0
N.8.85	18	720	507	458	12.2	21.2	0.34	0.86	759	0.028	−0.3	−16.0
N.8.88	2	6611	4236	981	12.6	61.9	0.09	0.66	761	0.004	−0.4	−16.0

than inherited cores in N.8.50, N.8.65 and N.8.68 but cores are still ~0.5. In N.8.51 and N.8.70, younger (~115 Ma) crystallisation exhibits low median Th/U values (0.21–0.25) compared to older zircon in those samples (median Th/U 0.50–0.78). Using [Ti], an average magmatic-age zircon from samples N.8.55, N.8.63, N.8.67 and N.8.70 (median [Ti] ~22 ppm) would have crystallised at ~813 °C, but lower [Ti] in N.8.50, N.8.51, N.8.65, N.8.68 and N.8.69 (median ~ 13 ppm) indicate crystallisation temperatures of ~765 °C. Most Eu/Eu* anomalies are very low (~0.06) except for N.8.51 and N.8.70 (0.42–0.46). According to Ce-U-Ti systematics, median ΔFMQ of samples are typically slightly negative but range from −2.8 (N.8.67) to +0.7 (N.8.69). Younger zircon in N.8.51 generally has lower ΔFMQ than inherited cores in that sample, but the distinction is not exclusive. This age-related trend is not apparent in N.8.70. Median absolute log(fO_2) values range from −16.5 to −14.7. The lowest absolute fO_2 is observed in N.8.51 and N.8.70 (−17.2 to −16.6) which also have the highest Eu/Eu* index.

5.11. Engel Peaks

Individual spot analyses on magmatic-age zircon in N.8.83, N.8.84 and N.8.85 from Engel Peaks contain concentrations of [U] between 449 and 5006 ppm, [Th] between 215 and 7926 ppm, [P] between 97 and 1798 ppm, [Ti] between 2 and 100 ppm, and [Ce] between 9 and 360 ppm. N.8.83 generally hosts higher concentrations of trace elements with a larger range than other Engel Peaks samples. For 95 % of spot analyses, concentrations of U, Th, P, Ti and Ce are less than 4310 ppm, 6270 ppm, 1430 ppm, 45 ppm and 220 ppm, respectively. In general, Engel Peaks zircon hosts greater trace element abundances than both Mount Faith and Sullivan. Only one valid spot analysis (N.8.84, spot 9) was categorised as an inherited core (1022 ± 34 Ma) where concentrations of U and Th are particularly low (100 ± 2 ppm and 59 ± 1 ppm, respectively). Ratios of Th/U range from 0.23 to 1.38, with a similar median Th/U for each sample between 0.90 and 0.93. Using median [Ti] in zircon for N.8.84 (~6 ppm) and N.8.85 (~12 ppm), crystallisation

temperatures would have been ~695 °C and ~ 759 °C, respectively. An average zircon of Ti-rich N.8.83 (median ~ 21 ppm) would have crystallised at ~811 °C. Europium concentrations were very low from these three samples ranging from 0.021 to 0.028. Median ΔFMQ surround zero or are slightly positive (−0.3 to 1.1) which reduce to absolute log (fO_2) of −16.1 to −15.8 using the Ti-in-zircon crystallisation temperatures.

N.8.88 from Engel Peaks, which hosts an evenly distributed age population of zircon from 181 to 497 Ma, exhibit zircon [U] between 1511 and 10,641 ppm, [Th] between 53 and 6698 ppm, [P] between 940 and 4657 ppm, [Ti] between 2 and 51 ppm and [Ce] between 0.7 and 70 ppm. Temporal trends exist in zircon from N.8.88; [U] increases and [Th] decreases with decreasing spot age, except for the two youngest spots (181.3 ± 5.8 Ma and 187.4 ± 5.7 Ma) with high [Th]. This means Th/U ratios tend to decrease from ~0.5 to ~0.01 with decreasing spot age, except for the two youngest spots that exhibit Th/U of 0.63–0.69 (Fig. 7). The [P] is lower in younger spots but still typical of S-type granites. Concentrations of Ce are generally lower in younger spots, except the youngest two samples. This means ΔFMQ also decreases from weakly negative (around −1) in older samples to strongly negative (around −6) in younger samples, except for the youngest two crystals which exhibit ΔFMQ ~0.

6. Discussion

6.1. Early Jurassic magmatism

The results of this work show that granitoids were emplaced at Mount Faith, Mount Sullivan, and Engel Peaks between 189 Ma and 179 Ma, with a peak of activity at ~184 Ma (Fig. 5, Table 4). These are the first geochronological constraints of the Mount Faith Granite and indicate that it is distinct from older Triassic (232 ± 4 Ma, whole-rock Rb—Sr) granitoids and younger mid-Jurassic (168 ± 1 Ma, whole-rock Rb—Sr) granitic intrusions of the Mount Charity Granite Complex 20 km south in the Eternity Range (Scarrow et al., 1996). This is also the first dedicated geological characterisation of the Mount Faith Granite. The calc-alkaline, weakly peraluminous, S-type *like* geochemistry as well as zircon chemistry and inheritance of older cores suggest that the Mount Faith Granite formed from partial melting of meta-igneous or meta-sedimentary protolith (Figs. 3, 5, and 6). This is typical of other Jurassic plutons compared to younger, less-fractionated plutons from lower crustal melts on the Peninsula (Wever et al., 1994). Although the Mount Faith Granite shares a similar composition to the mid-Jurassic granite at Mount Charity, the age of emplacement at Mount Faith is coeval with an earlier episode of Early Jurassic magmatism on the Peninsula (Bastias et al., 2021; Pankhurst et al., 2000; Riley et al., 2017). Additionally, U—Pb dating of zircon from the Mount Faith Granite provides an upper age constraint on cross-cutting tholeiitic dykes that previously were assumed to be of Triassic age after problematic Ar—Ar dating (Vaughan et al., 2012b).

Emplacement of the Mount Faith Granite during an episode of peak magmatism in the Early Jurassic could be related to the mantle plume 'flare-up' at 187–182 Ma that generated V1 Chon Aike silicic volcanics (Pankhurst et al., 2000) or arc magmatism associated with the Subcordilleran Plutonic Belt in Patagonia at 188–178 Ma (Bastias et al., 2021; Riley et al., 2017). It is more likely the Mount Faith Granite originates from the latter because of its volcanic arc geochemistry and S-like character (Figs. 3, 5 and 6) being similar to granitoids of the Subcordilleran Plutonic Belt (Navarrete et al., 2024; Rapela et al., 2005). Further, no other plutonic equivalent to the V1 Chon Aike volcanics have been identified on the Peninsula (Riley et al., 2017), although they are likely to be present at deeper crustal levels. Mid-Jurassic granites at Mount Charity are contemporaneous with V2 stage Chon Aike magmatism but are interpreted to be partial melts of metasedimentary crust which is unlike the character of V2 magmatism (Seitz et al., 2018). This could reflect local variation in melt source and magma mixing (Scarrow et al., 1996) or could be unrelated to Chon Aike magmatism.

New zircon U—Pb isotope data of granitoids from northeast Mount Sullivan indicate an Early Jurassic (188–184 Ma) crystallisation age which affirms one previous U—Pb zircon age (183 ± 3 Ma; Riley et al., 2017) but is slightly older than another whole-rock Rb—Sr age (178 ± 2 Ma; Pankhurst, 1983). Early Jurassic Mount Sullivan granitoids are calc-alkaline, peraluminous, ferroan, weakly S-type *like* with a volcanic arc signature and are moderately deformed (Figs. 3, 5, and 6). Such a signature suggests a magmatic arc source for Mount Sullivan granitoids associated with partial melting of meta-igneous to metasedimentary crust which is supported by previously measured Sr and Nd isotope signatures (Riley et al., 2017). Sample N.8.70 which is likely a mylonitised igneous rock hosts a population of ~180 Ma inherited zircon cores which likely represents the age of the main plutonic body (Fig. 5).

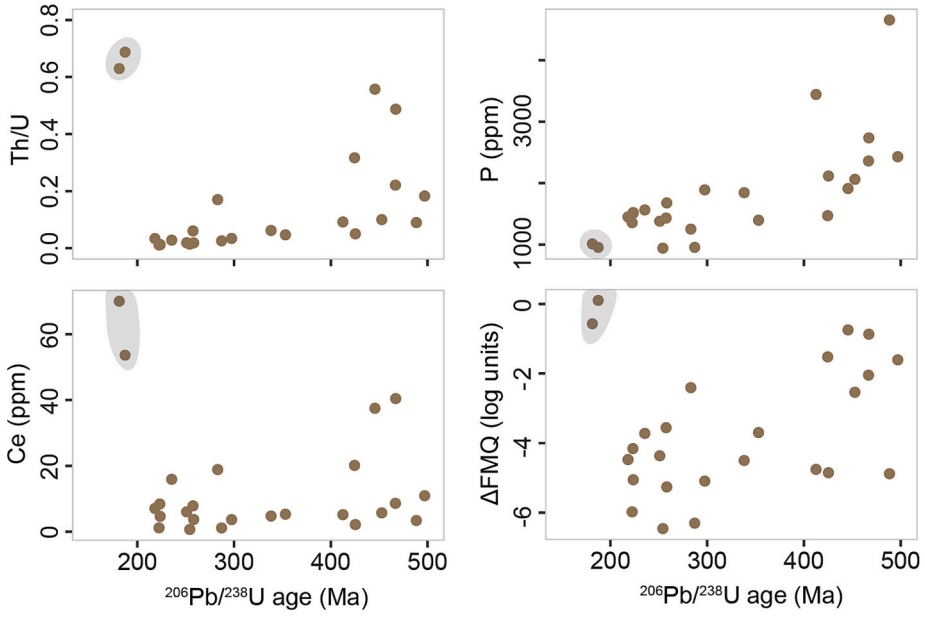

Fig. 7. Temporal trends in the trace element signature of zircon from N.8.88, with the most recent two Early Jurassic zircon crystals (grey region) showing relatively high Th/U, [Ce], and ΔFMQ, and [P] ~1000 ppm, which is similar to other zircon from the Engel Peaks Granite.

Field evidence of mafic and felsic magma mingling and suggests that the gabbro and granitoids of the main plutonic body crystallised synchronously (Vaughan et al., 2002). The timing of emplacement of granitoids here suggests a closer relationship to the contemporaneous Mount Faith Granite, rather than to mid-Jurassic granites at Mount Charity as previously suggested (Scarrow et al., 1996).

Data from this study shows that the crystallisation age of the granitic pluton exposed at Engel Peaks is also Early Jurassic (185–182 Ma), almost concordant with the one other robust age constraint available (188 ± 1 Ma, U—Pb zircon; Riley et al., 2017) and much older than an unpublished ~113 Ma age referred to by Meneilly et al. (1987). The younger age that is discussed in Meneilly et al. (1987) might represent age resetting during the Palmer Land Event (Vaughan et al., 2012a). The Engel Peaks Granite likely has the same magmatic origin as plutons at Mount Sullivan and Mount Faith given the similar crystallisation age (Fig. 5), zircon chemistry (Fig. 6), and isotopic makeup (Riley et al., 2017). XRD spectra and zircon petrochronology indicate that N.8.88 is a quartz-albite pegmatite generated from partial melting of a protolith containing Early Jurassic zircon similar that of Engel Peaks Granite as well as older inherited zircon (Fig. 7).

Trace element abundances in zircon vary across space for the Early Jurassic granitic plutons at Mount Faith, Mount Sullivan and Engel Peaks likely resulting from partial melting of different protoliths. Melts that formed the Mount Faith Granite were likely generated from more meta-igneous crust compared to partial melting of paragneisses and metasedimentary rocks found near Mount Sullivan and Engel Peaks (Meneilly et al., 1987; Vaughan et al., 2002). The concentration of REEs in zircon increase across present longitude from Mount Faith to Engel Peaks, which was parallel to the active subduction zone at the time of emplacement (Bastias et al., 2021; Jordan et al., 2020). There is no spatial trend in Al, Eu, Ti, and P concentrations, or the calculated crystallisation temperatures or oxygen fugacities. Hence, the variation in REE concentrations across space is not well explained by uptake kinetics because crystallisation temperature is invariant. The variation is also unlikely the result of differences in the degree of magma fractionation or redox state because both Eu/Eu* anomalies and calculated ΔFMQ are invariant (Loucks et al., 2020). The presence or absence of phases like monazite should sequester REEs before zircon, but incongruently monazite was more common in samples from Mount Sullivan where zircon is trace element-rich compared to Mount Faith. Therefore, it is most likely that the spatial differences in zircon REEs arise from melting of different crustal components. This also implies that the magma plumbing systems were likely related to long-lived subduction processes, potentially with magma pooling that assimilated upper crust, rather than to mantle-plume-related magmatism.

Several other plutons genetically related to the Subcordilleran Plutonic Belt, including Mount Faith, Mount Sullivan and Engel Peaks, outcrop as isolated nunataks along the Peninsula (Fig. 1; Riley et al., 2017). These are granitoids at the Eielson Peninsula and Mount Jackson further south in Palmer Land (Riley et al., 2017), at the Batterbee Mountains and Cape Bertreaux in eastern Palmer Land (Leat et al., 2009; Riley et al., 2017), and some in Graham Land (Riley et al., 2012; Riley et al., 2017). Equivalent plutons also outcrop in northern Patagonia where the Subcordilleran Plutonic Belt was first recognised (Navarrete et al., 2024; Rapela et al., 2005; Riley et al., 2017; Zaffarana et al., 2024). Together with new spatial and temporal constraints from this study, this supports widespread, coeval subduction-related magmatism across the Peninsula and Patagonia during the Early Jurassic. This will help refine models of complex tectonic activity and subduction processes during the early stages of Gondwana breakup. Contemporaneous, extension-related volcanism generated rhyolites and silicic ignimbrites of the Brennecke and Mount Poster Formations in southern Palmer Land but are considered part of the V1 volcanism of the Chon Aike silicic large igneous province rather than the Subcordilleran Plutonic Belt (Pankhurst et al., 2000; Riley et al., 2001; Riley et al., 2017).

6.2. Mid-Cretaceous recrystallisation related to the Palmer Land Event

Zircon from N.8.70 and N.8.51 at Mount Sullivan record mid-Cretaceous recrystallisation that produced 120.5 ± 1.2 Ma and 115.6 ± 1.0 Ma overgrowths, respectively (Fig. 5, Table 4). Inherited cores in N.8.70 zircon are ~180 Ma (Fig. 5), suggesting that 120.5 ± 1.2 Ma represents the age of recrystallisation of the Early Jurassic gabbroic protolith. Inherited cores in N.8.51 zircon surround ~180 Ma, suggesting that an Early Jurassic protolith was recrystallised at 115.6 ± 1.0 Ma (Fig. 5). Zircon trace element signatures in mid-Cretaceous-age zones are similar to Early Jurassic cores and other Mount Sullivan samples but have a distinct increase in [Eu] and Eu/Eu* index and decrease in [P], [Ce], Th/U, and relative oxygen fugacity (Fig. 6, Supplementary material 3). In addition to inherited Early Jurassic zircon and the presence of pyrite in a vein cross-cutting Early Jurassic granitoid N.8.69, this indicates that local crust was probably remelted under reducing conditions. Latest recrystallisation ages are ~10–15 Myr earlier than the peak of Phase 1 of the compressional PLE (~107 Ma; Vaughan et al., 2012b) but coincide with some of the earlier (Phase 1 and 2) granitoid crystallisation ages of the Lassiter Coast Intrusive Suite on the southern Peninsula (Riley et al., 2018; Vaughan et al., 2012a). This provides the first evidence outside of the Lassiter Coast Intrusive Suite that compressional deformation during the PLE began before ~116 Ma and as early as ~130 Ma (Riley et al., 2018).

6.3. Syn- and post-emplacement deformation and alteration

Petrographic and microstructural evidence of granitoids from Mount Faith indicate many have been deformed at relatively low-grade conditions. Aggregates of fine-scale, strain-free quartz with smoothly curved polygonal boundaries surrounding larger anhedral, interlobate quartz with undulose extinction (Fig. 2j) suggest partial recrystallisation by sub-grain rotation (Passchier and Trouw, 2005). Quartz microstructures like this form at moderate temperatures (400–500 °C), but a similar appearance could be formed by grain boundary migration at higher temperatures (>500 °C) if the temperature remained high after deformation had ceased (Stipp et al., 2002). Myrmekites in N.8.36 indicate deformation at ~600 °C (Passchier and Trouw, 2005), but brittle fracturing of feldspars in all samples (Fig. 2i) indicate low to medium temperature deformation 400–500 °C (Pryer, 1993). Hence, deformation of the Mount Faith granitoids likely occurred under a range of conditions from ~600 °C to low grade, submagmatic conditions at 400–450 °C.

The timing of deformation can be constrained by granite crystallisation ages and microscale petrological relationships measured here, as well as field relationships and Ar—Ar crystallisation ages of cross-cutting mafic dykes (Vaughan et al., 2012b). Tholeiitic mafic dykes with a minimum age of ~120 Ma cross-cut the ~184 Ma Mount Faith granite but do not exhibit a chilled margin. Calc-alkaline mafic dykes cross-cut both the granite and the tholeiitic dykes, commonly exhibit chilled margins, crystallised precisely at 100.3 ± 0.6 Ma, and are undeformed (Vaughan et al., 2012b). Therefore, two histories can be speculated. One possibility is that the granite was emplaced at ~184 Ma and deformed during cooling. Tholeiitic dykes intruded before thermal equilibration of the granitoid and deformed either during or after granite deformation (Vaughan et al., 2012b). Tholeiitic dykes could be related to a dyke swarm at ~178 Ma (Riley et al., 2016) associated with Weddell Sea rifting. Calc-alkaline dykes then intruded at ~100 Ma. A second possibility it that the granite completely cooled before tholeiitic dykes intruded, then regional-scale deformation occurred before calc-alkaline dykes intruded at ~100 Ma. In the latter scenario, heat flow during emplacement of the tholeiitic dykes must have been sustained so that chilled margins did not develop (Huppert and Sparks, 1989). Correlative granitoids of the Subcordilleran Plutonic Belt all exhibit foliation which could be related to marginal strain during emplacement (Millar et al., 2002; Riley et al., 2017). If the Mount Faith Granite

deformed during emplacement like other granitoids of the Subcordilleran Plutonic Belt, the first scenario is more likely that tholeiitic dykes must have intruded before thermal equilibration and deformation.

Further, Mount Faith granitoids exhibit characteristics of hydrothermal alteration which is widespread across the Peninsula (Pankhurst, 1982; Thomson and Pankhurst, 1983). Plagioclase alteration to sericite and epidote group minerals like clinozoisite as well as partial replacement of biotite to chlorite (Fig. 2m) indicate hydrothermal alteration under low-grade metamorphic conditions (Leichmann et al., 2003). Chlorite replacement of biotite typically occurs in isochemical (or slightly Fe—Mg enriched) hydrothermal fluids at 200–300 °C (Parneix et al., 1985). This could be related to either episode of dyke intrusion (Vaughan et al., 2012b) or post crystallisation deformation. The development of leucoxene coronas on ilmenite could be a result of weak interaction with intrusion-related hydrothermal fluids (Whalen and Chappell, 1988) or surface weathering (Mücke and Bhadra Chaudhuri, 1991).

Mount Sullivan exhibits higher grade deformation than is observed at Mount Faith. The quartz has been completely recrystallised and is anhedral with interlobate to amoeboid boundaries, seriate, and does not feature undulose extinction (Fig. 2n). This indicates deformation at high temperatures (>500 °C; Stipp et al., 2002). The presence of flame perthite (Fig. 2n) indicates greenschist facies conditions and is commonly found in ductile shear zones (Debat et al., 1978). These observations are expected for rocks affected by high-temperature ductile deformation of the mid-Cretaceous PLE (Vaughan et al., 2012a), but may have been originally strained to some degree during emplacement like other Subcordilleran plutons (Millar et al., 2002; Riley et al., 2017).

7. Conclusions

Whole-rock geochemistry and zircon petrochronology provide detailed new geological descriptions and reveal the timing and source of granitoid genesis for archived samples from northeast Palmer Land, Antarctic Peninsula. Novel analyses of bedrock at Mount Faith show it is largely a calc-alkaline, peraluminous, ferroan, S-type *like* granite (sensu stricto) that crystallised 189–179 Ma under typical magmatic temperatures (~780 °C) and a neutral oxygen fugacity (ΔFMQ = −0.1, fO_2 = −15.4). While contemporaneous with V1 Chon Aike volcanics, its emplacement is more likely related to the Subcordilleran Plutonic Belt. The Mount Faith Granite is distinct from the three generations of granite at Mount Charity. It is weakly deformed, hydrothermally altered, and cross-cut by two generations of mafic dykes, all of which now have an upper age constraint. However, precise timing of deformation is unconstrained between ~184 and ~ 100 Ma and could be due to *syn*-emplacement strain or post-emplacement regional deformation.

Bedrock at Mount Sullivan is diverse. Rocks analysed here from the northeastern spur of Mount Sullivan are mostly felsic plutonic members of a mingled gabbroic-granitic parent magma influenced by anatexis of local metasedimentary rocks, and new zircon U—Pb dating indicate crystallisation between 188 and 184 Ma. Available whole-rock samples and mineralogy of crushed separates indicate these were granites (sensu stricto) that were later deformed by the mid-Cretaceous PLE. Crystallisation conditions of Early Jurassic rocks (~790 °C, ΔFMQ = −0.4, fO_2 = −15.4) are similar to the Mount Faith Granite and probably also related to magmatism of the Subcordilleran Plutonic Belt. Zircon recrystallisation at 120.5 ± 1.2 Ma and 115.6 ± 1.0 Ma provide the earliest expression of the PLE outside of the related Lassiter Coast Intrusive Suite.

Finely crushed rock and zircon chemistry from the Engel Peaks Granite indicate S-type *like* granitic host rock and related pegmatites from partial melting of metasedimentary crust. New zircon U—Pb dating here reveals Early Jurassic crystallisation 185–182 Ma. The pluton is likely related to other plutons of the Subcordilleran Plutonic Belt (Riley et al., 2017). Major faulting and associated deformation are likely related to the Early Cretaceous PLE.

New constraints for the timing and source of magmatism in northeast Palmer Land will be useful for precise plate reconstructions of southwestern Gondwana during the Early Jurassic. Also, the new bulk rock and zircon dataset provides a detailed geochemical and chronological 'fingerprint' of bedrock at Mount Faith, Mount Sullivan, and Engel Peaks. A matching fingerprint could be used to identify moraine or till provenance downstream and therefore reconstruct ice flow pathways (e.g., Agrios et al., 2022). Detrital zircon recovered from the Weddell Sea with an Early Jurassic fingerprint that matches these sites could help distinguish sediment provenance from other bedrock on the Peninsula or sources further afield like East Antarctica (e.g., Veevers and Saeed, 2013).

Although archived samples were useful for geochronological analyses here, future fieldwork to northeast Palmer Land should focus on recording field relationships of these samples to validate interpretations. Additional sampling of distinct lithologies surrounding Mount Faith, Mount Sullivan, and Engel Peaks for in situ zircon U—Pb dating would improve the understanding of the timing of emplacement and subsequent metamorphic history. Whole-rock Sr and Nd isotope signatures or additional zircon trace element 'fingerprinting' could confirm similarity to plutons of the Subcordilleran belt. Fingerprinting work of bedrock on the Peninsula could be extended and applied to provenance analysis of moraines or offshore sediments to reconstruct former ice flow.

CRediT authorship contribution statement

Ryan North: Writing – review & editing, Writing – original draft, Visualization, Methodology, Investigation, Funding acquisition, Formal analysis, Data curation, Conceptualization. **Lloyd T. White:** Writing – review & editing, Supervision, Resources, Methodology, Funding acquisition, Conceptualization. **Teal R. Riley:** Writing – review & editing, Resources, Methodology, Conceptualization. **Dominique Tanner:** Writing – review & editing, Resources, Methodology, Conceptualization. **Timothy T. Barrows:** Writing – review & editing, Supervision, Resources, Project administration, Methodology, Funding acquisition, Conceptualization.

Declaration of competing interest

The authors declare that they have no known competing financial interests or personal relationships that could have appeared to influence the work reported in this paper.

Acknowledgements

We are grateful for Rebecca Rixon (University of Exeter) for the original sample collection, Mark Evans (BAS) for sample curation and access, Allen Nutman (UOW) for assisting with zircon preparation, Mitchell Nancarrow (UOW) for helping collect zircon CL imagery, José Abrantes (UOW) for preparing samples for XRF, Alan Vaughan for providing original field notes and photographs, and two anonymous reviewers. This work was enabled by use of the Central Analytical Research Facility (CARF) at the Queensland University of Technology (QUT) and we thank Mitchell De Bruyn and Charlotte Allen for collecting zircon geochemical data. This work was supported by ARC SRIEAS Grant SR200100005 Securing Antarctica's Environmental Future.

Appendix A. Supplementary data

Supplementary data to this article can be found online at https://doi.org/10.1016/j.lithos.2025.108188.

References

Agrios, L.M., Licht, K.J., Williams, T., Hemming, S.R., Welch, L., Mickey, J.L., 2022. Detrital geochronology and lithologic signatures of Weddell Sea Embayment ice streams, Antarctica—implications for subglacial geology and ice sheet history. Bull. Geol. Soc. Am. 134, 1895–1915. https://doi.org/10.1130/B36117.1.

Bastias, J., Spikings, R., Riley, T., Ulianov, A., Grunow, A., Chiaradia, M., Hervé, F., 2021. A revised interpretation of the Chon Aike magmatic province: active margin origin and implications for the opening of the Weddell Sea. Lithos 386–387, 1. https://doi.org/10.1016/j.lithos.2021.106013.

Bastias, J., Spikings, R., Riley, T., Chew, D., Grunow, A., Ulianov, A., Chiaradia, M., Burton-Johnson, A., 2022. Cretaceous magmatism in the Antarctic Peninsula and its tectonic implications. J. Geol. Soc. Lond. 180, 1–18. https://doi.org/10.6084/m9.figshare.c.6089274.

Belousova, E.A., Griffin, W.L., O'Reilly, S.Y., Fisher, N.I., 2002. Igneous zircon: trace element composition as an indicator of source rock type. Contrib. Mineral. Petrol. 143, 602–622. https://doi.org/10.1007/s00410-002-0364-7.

Belousova, E.A., Griffin, W.L., O'Reilly, S.Y., 2006. Zircon crystal morphology, trace element signatures and Hf isotope composition as a tool for petrogenetic modelling: examples from Eastern Australian granitoids. J. Petrol. 47, 329–353. https://doi.org/10.1093/petrology/egi077.

Black, L.P., Kamo, S.L., Allen, C.M., Davis, D.W., Aleinikoff, J.N., Valley, J.W., Mundil, R., Campbell, I.H., Korsch, R.J., Williams, I.S., Foudoulis, C., 2004. Improved 206Pb/238U microprobe geochronology by the monitoring of a trace-element-related matrix effect; SHRIMP, ID-TIMS, ELA-ICP-MS and oxygen isotope documentation for a series of zircon standards. Chem. Geol. 205, 115–140. https://doi.org/10.1016/j.chemgeo.2004.01.003.

British Antarctic Survey, 1967. Interim geological report: East coast 1965-67. Reproduced Courtesy of BAS Archives Service. Archives Ref. AD6/2E/1966/G2. Copyright: UKRI-BAS.

British Antarctic Survey, 1971a. Interim geological report: field report on the reconnaissance geological survey of the west coast of Palmer Land - Meiklejohn Glacier to Eureka Glacier, George VI Sound side; also western sides of Mount Faith and Mount Hope, Eternity Range. Reproduced Courtesy of BAS Archives Service. Archives Ref. AD6/2E/1970/G5. Copyright: UKRI-BAS.

British Antarctic Survey, 1971b. Interim report: the geology of Mount Charity, the eastern side of Mounts Hope and Faith, and eastwards through Mount Sullivan to Engel Peaks. Reproduced Courtesy of BAS Archives Service. Archives Ref. AD6/2E/1971/G5. Copyright: UKRI-BAS.

British Antarctic Survey, 1989. Geological field observations in northeastern Palmer Land. Field report: 1988-89 season. Reproduced Courtesy of BAS Archives Service. Archives Ref. AD6/2R/1988/G5. Copyright: UKRI-BAS.

British Antarctic Survey, 2002. Geological observations from North-eastern Palmer Land localities, including the Welch Mountains, Clark Hills, Hall Ridge, Pinther Ridge, and Eternity Range areas, 2001/2002 season. Reproduced Courtesy of BAS Archives Service. Archives Ref. AD6/2R/2001/GL2. Copyright: UKRI-BAS.

Burnham, A.D., Berry, A.J., 2017. Formation of Hadean granites by melting of igneous crust. Nat. Geosci. 10, 457–461. https://doi.org/10.1038/ngeo2942.

Burton-Johnson, A., Riley, T.R., 2015. Autochthonous v. accreted terrane development of continental margins: a revised in situ tectonic history of the Antarctic Peninsula. J. Geol. Soc. Lond. 172, 822–835. https://doi.org/10.1144/jgs2014-110.

Chappell, B.W., White, A.J.R., 1992. I- and S-type granites in the Lachlan fold belt. Trans. R. Soc. Edinb. Earth Sci. 83, 1–26. https://doi.org/10.1017/S0263593300007720.

Cox, S.C., Smith Lyttle, B., Elkind, S., Smith Siddoway, C., Morin, P., Capponi, G., Abu-Alam, T., Ballinger, M., Bamber, L., Kitchener, B., Lelli, L., Mawson, J., Millikin, A., Dal Seno, N., Whitburn, L., White, T., Burton-Johnson, A., Crispini, L., Elliot, D., Elvevold, S., Goodge, J., Halpin, J., Jacobs, J., Martin, A.P., Mikhalsky, E., Morgan, F., Scadden, P., Smellie, J., Wilson, G., 2023. A continent-wide detailed geological map dataset of Antarctica. Sci Data 10, 1–14. https://doi.org/10.1038/s41597-023-02152-9.

Davies, T.G., 1984. The geology of part of Northern Palmer Land. In: British Antarctic Survey Scientific Reports.

Debat, P., Soula, J.-C., Kubin, L., Vidal, J.-L., 1978. Optical studies of natural deformation microstructures in feldspars (gneiss and pegmatites from Occitania, southern France). Lithos 11, 133–145. https://doi.org/10.1016/0024-4937(78)90004-X.

Frost, B.R., Barnes, C.G., Collins, W.J., Arculus, R.J., Ellis, D.J., Frost, C.D., 2001. A geochemical classification for granitic rocks. J. Petrol. 42, 2033–2048. https://doi.org/10.1093/petrology/42.11.2033.

Gao, L., Pei, J., Zhao, Y., Yang, Z., Riley, T.R., Liu, X., Zhang, S.H., Liu, J.M., 2021. New paleomagnetic constraints on the Cretaceous tectonic framework of the Antarctic Peninsula. J. Geophys. Res. Solid Earth 126, 1–17. https://doi.org/10.1029/2021JB022503.

Horstwood, M.S.A., Košler, J., Gehrels, G., Jackson, S.E., McLean, N.M., Paton, C., Pearson, N.J., Sircombe, K., Sylvester, P., Vermeesch, P., Bowring, J.F., Condon, D.J., Schoene, B., 2016. Community-derived standards for LA-ICP-MS U-(Th-)Pb geochronology – uncertainty propagation, age interpretation and data reporting. Geostand. Geoanal. Res. 40, 311–332. https://doi.org/10.1111/j.1751-908X.2016.00379.x.

Huppert, H.E., Sparks, R.S.J., 1989. Chilled margins in igneous rocks. Earth Planet. Sci. Lett. 92, 397–405. https://doi.org/10.1016/0012-821X(89)90063-0.

Ivanov, A.V., Meffre, S., Thompson, J., Corfu, F., Kamenetsky, V.S., Kamenetsky, M.B., Demonterova, E.I., 2017. Timing and genesis of the Karoo-Ferrar large igneous province: new high precision U-Pb data for Tasmania confirm short duration of the major magmatic pulse. Chem. Geol. 455, 32–43. https://doi.org/10.1016/j.chemgeo.2016.10.008.

Jackson, S.E., Pearson, N.J., Griffin, W.L., Belousova, E.A., 2004. The application of laser ablation-inductively coupled plasma-mass spectrometry to in situ U-Pb zircon geochronology. Chem. Geol. 211, 47–69. https://doi.org/10.1016/j.chemgeo.2004.06.017.

Jochum, K.P., Weis, U., Schwager, B., Stoll, B., Wilson, S.A., Haug, G.H., Andreae, M.O., Enzweiler, J., 2016. Reference values following ISO guidelines for frequently requested rock reference materials. Geostand. Geoanal. Res. 40, 333–350. https://doi.org/10.1111/j.1751-908X.2015.00392.x.

Jordan, T.A., Neale, R.F., Leat, P.T., Vaughan, A.P.M., Flowerdew, M.J., Riley, T.R., Whitehouse, M.J., Ferraccioli, F., 2014. Structure and evolution of Cenozoic arc magmatism on the Antarctic Peninsula: a high resolution aeromagnetic perspective. Geophys. J. Int. 198, 1758–1774. https://doi.org/10.1093/gji/ggu233.

Jordan, T.A., Riley, T.R., Siddoway, C.S., 2020. The geological history and evolution of West Antarctica. Nat. Rev. Earth Environ. https://doi.org/10.1038/s43017-019-0013-6.

Kirkland, C.L., Smithies, R.H., Taylor, R.J.M., Evans, N., McDonald, B., 2015. Zircon Th/U ratios in magmatic environs. Lithos 212–215, 397–414. https://doi.org/10.1016/j.lithos.2014.11.021.

Leat, P.T., Scarrow, J.H., Millar, I.L., 1995. On the Antarctic Peninsula batholith. Geol. Mag. 132, 399–412. https://doi.org/10.1017/S0016756800021464.

Leat, P.T., Flowerdew, M.J., Riley, T.R., Whitehouse, M.J., Scarrow, J.H., Millar, I.L., 2009. Zircon U-Pb dating of Mesozoic volcanic and tectonic events in North-West Palmer Land and South-West Graham Land, Antarctica. Antarct. Sci. 21, 633–641. https://doi.org/10.1017/S0954102009990320.

Leichmann, J., Broska, I., Zachovalová, K., 2003. Low-grade metamorphic alteration of feldspar minerals: a CL study. Terra Nova 15, 104–108. https://doi.org/10.1046/j.1365-3121.2003.00467.x.

Loucks, R.R., Fiorentini, M.L., Henriquez, G.J., 2020. New magmatic oxybarometer using trace elements in zircon. J. Petrol. 61, 1–30. https://doi.org/10.1093/petrology/egaa034.

McDonough, W.F., Sun, S.-S., 1995. The composition of the Earth. Chem. Geol. 120, 223–253. https://doi.org/10.1016/0009-2541(94)00140-4.

Meneilly, A.W., 1988. Reverse fault step at Engel Peaks, Antarctic Peninsula. J. Struct. Geol. 10, 393–403. https://doi.org/10.1016/0191-8141(88)90017-X.

Meneilly, A.W., Harrison, S.M., Piercy, B.A., Storey, B.C., 1987. Structural evolution of the magmatic arc in Northern Palmer Land, Antarctic Peninsula. In: Gondwana Six: Structure, Tectonics, and Geophysics. American Geophysical Union, pp. 209–219. https://doi.org/10.1029/gm040p0209.

Middlemost, E.A.K., 1994. Naming materials in the magma/igneous rock system. Earth Sci. Rev. 37, 215–224. https://doi.org/10.1016/0012-8252(94)90029-9.

Millar, I.L., Pankhurst, R.J., Fanning, C.M., 2002. Basement chronology of the Antarctic Peninsula: recurrent magmatism and anatexis in the Palaeozoic Gondwana margin. J. Geol. Soc. Lond. 159, 145–157. https://doi.org/10.1144/0016-764901-020.

Mücke, A., Bhadra Chaudhuri, J.N., 1991. The continuous alteration of ilmenite through pseudorutile to leucoxene. Ore Geol. Rev. 6, 25–44. https://doi.org/10.1016/0169-1368(91)90030-B.

Navarrete, C., Gianni, G., Tassara, S., Zaffarana, C., Likerman, J., Márquez, M., Wostbrock, J., Planavsky, N., Tardani, D., Perez Frasette, M., 2024. Massive Jurassic slab break-off revealed by a multidisciplinary reappraisal of the Chon Aike silicic large igneous province. Earth Sci. Rev. 249. https://doi.org/10.1016/j.earscirev.2023.104651.

Pankhurst, R.J., 1982. Rb-Sr geochronology of Graham Land, Antarctica. J. Geol. Soc. Lond. 139, 701–711. https://doi.org/10.1144/gsjgs.139.6.0701.

Pankhurst, R.J., 1983. Rb-Sr constraints on the ages of basement rocks of the Antarctic Peninsula. In: Oliver, R.L., Jame, P.R., Jago, J.B. (Eds.), Antarctic Earth Science. Australian Academy of Science, Cambridge University Press, Canberra, Cambridge, pp. 367–371.

Pankhurst, R.J., Leat, P.T., Sruoga, P., Rapela, C.W., Marquez, M., Storey, B.C., Riley, T.R., 1998. The Chon Aike province of Patagonia and related rocks in West Antarctica: a silicic large igneous province. J. Volcanol. Geotherm. Res. https://doi.org/10.1016/S0377-0273(97)00070-X.

Pankhurst, R.J., Riley, T.R., Fanning, C.M., Kelley, S.P., 2000. Episodic silicic volcanism in Patagonia and the Antarctic Peninsula: chronology of magmatism associated with the break-up of Gondwana. J. Petrol. 41, 605–625. https://doi.org/10.1093/petrology/41.5.605.

Parneix, J.C., Beaufort, D., Dudoignon, P., Meunier, A., 1985. Biotite chloritization process in hydrothermally altered granites. Chem. Geol. https://doi.org/10.1016/0009-2541(85)90089-0.

Passchier, C.W., Trouw, R.A., 2005. Microtectonics. Springer Science & Business Media. https://doi.org/10.1007/3-540-29359-0.

Paterson, S.R., Ducea, M.N., 2015. Arc magmatic tempos: gathering the evidence. Elements 11, 91–98. https://doi.org/10.2113/gselements.11.2.91.

Paton, C., Hellstrom, J., Paul, B., Woodhead, J., Hergt, J., 2011. Iolite: freeware for the visualisation and processing of mass spectrometric data. J. Anal. At. Spectrom. 26, 2508–2518. https://doi.org/10.1039/c1ja10172b.

Paul, B., Petrus, J., Savard, D., Woodhead, J., Hergt, J., Greig, A., Paton, C., Rayner, P., 2023. Time resolved trace element calibration strategies for LA-ICP-MS. J. Anal. At. Spectrom. 38, 1995–2006. https://doi.org/10.1039/d3ja00037k.

Pearce, J.A., Harris, N.B.W., Tindle, A.G., 1984. Trace element discrimination diagrams for the tectonic interpretation of granitic rocks. J. Petrol. 25, 956–983. https://doi.org/10.1093/petrology/25.4.956.

Petrus, J.A., Kamber, B.S., 2012. VizualAge: a novel approach to laser ablation ICP-MS U-Pb geochronology data reduction. Geostand. Geoanal. Res. 36, 247–270. https://doi.org/10.1111/j.1751-908X.2012.00158.x.

Pryer, L.L., 1993. Microstructures in feldspars from a major crustal thrust zone: the Grenville Front, Ontario, Canada. J. Struct. Geol. 15, 21–26. https://doi.org/10.1016/0191-8141(93)90076-M.

Rapela, C.W., Pankhurst, R.J., Fanning, C.M., Hervé, F., 2005. Pacific subduction coeval with the Karoo mantle plume: the Early Jurasssic Subcordilleran belt of northwestern Patagonia. Geol. Soc. Lond. Spec. Publ. 246, 217–239. https://doi.org/10.1144/GSL.SP.2005.246.01.07.

Riley, T.R., Leat, P.T., Pankhurst, R.J., Harris, C., 2001. Origins of large volume rhyolitic volcanism in the Antarctic Peninsula and Patagonia by crustal melting. J. Petrol. 42, 1043–1065. https://doi.org/10.1093/petrology/42.6.1043.

Riley, T.R., Flowerdew, M.J., Whitehouse, M.J., 2012. U-Pb ion-microprobe zircon geochronology from the basement inliers of eastern Graham Land, Antarctic Peninsula. J. Geol. Soc. Lond. 169, 381–393. https://doi.org/10.1144/0016-76492011-142.

Riley, T.R., Curtis, M.L., Flowerdew, M.J., Whitehouse, M.J., 2016. Evolution of the Antarctic Peninsula lithosphere: evidence from Mesozoic mafic rocks. Lithos 244, 59–73. https://doi.org/10.1016/j.lithos.2015.11.037.

Riley, T.R., Flowerdew, M.J., Pankhurst, R.J., Curtis, M.L., Millar, I.L., Fanning, C.M., Whitehouse, M.J., 2017. Early Jurassic magmatism on the Antarctic Peninsula and potential correlation with the Subcordilleran plutonic belt of Patagonia. J. Geol. Soc. Lond. 174, 365–376. https://doi.org/10.6084/m9.figshare.c.3521973.

Riley, T.R., Burton-Johnson, A., Flowerdew, M.J., Whitehouse, M.J., 2018. Episodicity within a Mid-Cretaceous Magmatic Flare-Up in West Antarctica: U-Pb Ages of the Lassiter Coast Intrusive Suite, Antarctic Peninsula, and Correlations Along the Gondwana Margin. https://doi.org/10.1130/B31800.1.

Riley, T.R., Flowerdew, M.J., Burton-Johnson, A., Leat, P.T., Millar, I.L., Whitehouse, M. J., 2020. Cretaceous arc volcanism of Palmer Land, Antarctic Peninsula: zircon U-Pb geochronology, geochemistry, distribution and field relationships. J. Volcanol. Geotherm. Res. 401. https://doi.org/10.1016/j.jvolgeores.2020.106969.

Riley, T.R., Burton-Johnson, A., Flowerdew, M.J., Poblete, F., Castillo, P., Hervé, F., Leat, P.T., Millar, I.L., Bastias, J., Whitehouse, M.J., 2023. Palaeozoic – early Mesozoic geological history of the Antarctic Peninsula and correlations with Patagonia: kinematic reconstructions of the proto-Pacific margin of Gondwana. Earth Sci. Rev. https://doi.org/10.1016/j.earscirev.2022.104265.

Scarrow, J.H., Pankhurst, R.J., Leat, P.T., Vaughan, A.P.M., 1996. Antarctic Peninsula granitoid petrogenesis: a case study from Mount charity, North-Eastern Palmer Land. Antarct. Sci. 8, 193–206. https://doi.org/10.1017/s0954102096000260.

Seitz, S., Putlitz, B., Baumgartner, L.P., Bouvier, A.S., 2018. The role of crustal melting in the formation of rhyolites: constraints from SIMS oxygen isotope data (Chon Aike Province, Patagonia, Argentina). Am. Mineral. 103, 2011–2027. https://doi.org/10.2138/am-2018-6520.

Sláma, J., Košler, J., Condon, D.J., Crowley, J.L., Gerdes, A., Hanchar, J.M., Horstwood, M.S.A., Morris, G.A., Nasdala, L., Norberg, N., Schaltegger, U., Schoene, B., Tubrett, M.N., Whitehouse, M.J., 2008. Plešovice zircon - a new natural reference material for U-Pb and Hf isotopic microanalysis. Chem. Geol. 249, 1–35. https://doi.org/10.1016/j.chemgeo.2007.11.005.

Stipp, M., Stünitz, H., Heilbronner, R., Schmid, S.M., 2002. The eastern Tonale fault zone: a "natural laboratory" for crystal plastic deformation of quartz over a temperature range from 250 to 700 °C. J. Struct. Geol. 24, 1861–1884. https://doi.org/10.1016/S0191-8141(02)00035-4.

Taylor, S.R., McLennan, S., 1985. Continental crust: its composition and evolution. In: An Examination of the Geochemical Record Preserved in Sedimentary Rocks. Blackwell Scientific, Oxford, p. 312. https://doi.org/10.1017/S0016756800032167.

Thomson, M.R.A., Pankhurst, R.J., 1983. Age of post-Gondwanian calc-alkaline volcanism in the Antarctic Peninsula region. In: Oliver, R.L., Jame, P.R., Jago, J.B. (Eds.), Antarctic Earth Science. Australian Academy of Science, Cambridge University Press, Canberra, Cambridge, pp. 328–333.

Trail, D., Bruce Watson, E., Tailby, N.D., 2012. Ce and Eu anomalies in zircon as proxies for the oxidation state of magmas. Geochim. Cosmochim. Acta 97, 70–87. https://doi.org/10.1016/j.gca.2012.08.032.

Vaughan, A.P.M., Storey, B.C., 2000. The eastern Palmer Land shear zone: a new terrane accretion model for the Mesozoic development of the Antarctic Peninsula. J. Geol. Soc. Lond. 157, 1243–1256. https://doi.org/10.1144/jgs.157.6.1243.

Vaughan, A.P.M., Kelley, S.P., Storey, B.C., 2002. Mid-Cretaceous ductile deformation on the Eastern Palmer Land Shear Zone, Antarctica, and implications for timing of Mesozoic terrane collision. Geol. Mag. 139, 465–471. https://doi.org/10.1017/S0016756802006672.

Vaughan, A.P.M., Eagles, G., Flowerdew, M.J., 2012a. Evidence for a two-phase Palmer Land event from crosscutting structural relationships and emplacement timing of the Lassiter Coast Intrusive Suite, Antarctic Peninsula: implications for mid-Cretaceous Southern Ocean plate configuration. Tectonics. https://doi.org/10.1029/2011TC003006.

Vaughan, A.P.M., Leat, P.T., Dean, A.A., Millar, I.L., 2012b. Crustal thickening along the West Antarctic Gondwana margin during mid-Cretaceous deformation of the Triassic intra-oceanic Dyer Arc. Lithos 142–143, 130–147. https://doi.org/10.1016/j.lithos.2012.03.008.

Veevers, J.J., Saeed, A., 2013. Age and composition of Antarctic sub-glacial bedrock reflected by detrital zircons, erratics, and recycled microfossils in the Ellsworth Land-Antarctic Peninsula-Weddell Sea-Dronning Maud Land sector (240°E-0°-015°E). Gondwana Res. 23, 296–332. https://doi.org/10.1016/j.gr.2012.05.010.

Vermeesch, P., 2018. IsoplotR: a free and open toolbox for geochronology. Geosci. Front. 9, 1479–1493. https://doi.org/10.1016/j.gsf.2018.04.001.

Vermeesch, P., 2021. On the treatment of discordant detrital zircon U-Pb data. Geochronology 3, 247–257. https://doi.org/10.5194/gchron-3-247-2021.

Watson, E.B., Wark, D.A., Thomas, J.B., 2006. Crystallization thermometers for zircon and rutile. Contrib. Mineral. Petrol. 151, 413–433. https://doi.org/10.1007/s00410-006-0068-5.

Wever, H.E., Millar, I.J., Pankhurst, R.J., 1994. Geochronology and radiogenic isotope geology of Mesozoic rocks from eastern Palmer Land, Antarctic Peninsula: crustal anatexis in arc-related granitoid genesis. J. S. Am. Earth Sci. 7, 69–83. https://doi.org/10.1016/0895-9811(94)90035-3.

Whalen, J.B., Chappell, B.W., 1988. Opaque mineralogy and mafic mineral chemistry of I-and S-type granites of the Lachlan fold belt, Southeast Australia. Am. Mineral. 73, 281–296.

Wiedenbeck, M., Alle, P., Corfu, F., Griffin, W.L., Meier, M., Oberli, F., Von Quadt, A., Roddick, J.C., Spiegel, W., 1995. Three natural zircon standards for U-Th-Pb, Lu-Hf, trace element and REE analyses. Geostand. Newslett. 19, 1–23. https://doi.org/10.1111/j.1751-908X.1995.tb00147.x.

Yakymchuk, C., Kirkland, C.L., Clark, C., 2018. Th/U ratios in metamorphic zircon. J. Metamorph. Geol. 36, 715–737. https://doi.org/10.1111/jmg.12307.

Yakymchuk, C., Holder, R.M., Kendrick, J., Moyen, J.F., 2023. Europium anomalies in zircon: a signal of crustal depth? Earth Planet. Sci. Lett. 622, 1–11. https://doi.org/10.1016/j.epsl.2023.118405.

Zaffarana, C.B., Orts, D., Gallastegui, G., Suárez, R., Poma, S., Pernich, S., Aramendía, B., 2024. Reviewing the geochemistry and petrology of the subcordilleran plutonic belt, early Jurassic magmatic arc in northern Patagonia. J. S. Am. Earth Sci. 145, 1–23. https://doi.org/10.1016/j.jsames.2024.105065.